JM PAPERS

CrossMark

Reactive control of second Mack mode in a supersonic boundary layer with free-stream velocity/density variations

Pierre Nibourel[1],†, **Colin Leclercq**[1], **Fabrice Demourant**[2], **Eric Garnier**[1] and **Denis Sipp**[1]

[1]ONERA-DAAA, Université Paris-Saclay, 8 Rue des Vertugadins, 92190 Meudon, France

[2]ONERA-DTIS, 2 Avenue Edouard Belin, 31000 Toulouse, France

We consider closed-loop control of a two-dimensional supersonic boundary layer at $M = 4.5$ that aims at reducing the linear growth of second Mack mode instabilities. These instabilities are first characterized with local spatial and global resolvent analyses, which allow us to refine the control strategy and to select appropriate actuators and sensors. After linear input–output reduced-order models have been identified, multi-criteria structured mixed H_2/H_∞ synthesis allows us to fix beforehand the controller structure and to minimize appropriate norms of various transfer functions: the H_2 norm to guarantee performance (reduction of perturbation amplification in nominal condition), and the H_∞ norm to maintain performance robustness (with respect to sensor noise) and stability robustness (with respect to uncertain free-stream velocity/density variations). Both feedforward and feedback set-ups, i.e. with estimation sensor placed respectively upstream/downstream of the actuator, allow us to maintain the local perturbation energy below a given threshold over a significant distance downstream of the actuator, even in the case of noisy estimation sensors or free-stream density variations. However, the feedforward set-up becomes completely ineffective when convective time delays are altered by free-stream velocity variations of $\pm 5\,\%$, which highlights the strong relevance of the feedback set-up for performance robustness in convectively unstable flows.

Key words: boundary layer control, boundary layer stability, instability control

1. Introduction

Transition to turbulence in a boundary layer results in increased wall friction, penalizing aircraft drag. At high speeds, the generated heat is significant and becomes a major

† Email address for correspondence: pierre.nibourel@onera.fr

concern for the design of supersonic/hypersonic vehicles (Juliano, Borg & Schneider 2015). The transition to turbulence in boundary layers is initiated by amplification of external disturbances of various kinds (roughness, sound waves, free-stream turbulence, etc.), and several paths to transition are possible depending on the nature and intensity of incoming disturbances (Morkovin 1969). With low levels of disturbances, their growth is described by linear stability theory. The stability of a supersonic boundary layer has been studied widely in the literature (Mack 1984; Malik 1989; Ma & Zhong 2003; Bugeat *et al.* 2019; and many others). For sufficiently high Mach numbers, this configuration is characterized by the presence of two distinct inviscid instability mechanisms: a generalized inflection point for the first Mack mode (Mack 1984), and a region where the streamwise base-flow velocity relative to the disturbance phase velocity is supersonic for the second Mack mode, implying that acoustic noise is trapped in this region (Mack 1984; Fedorov 2011). A classical approach for relating instability to transition is based precisely on this linear framework and is called the *N*-factor method (Smith & Gamberoni 1956), wherein transition is assumed to occur when a perturbation has been amplified by a factor e^N, which defines an energy threshold depending on the disturbance environment.

Numerous studies addressed the problem of transition delay in the supersonic boundary layer flow using active control: Gaponov & Smorodsky (2016) injected heavy gas through porous wall to reduce surface friction and heat transfer, Sharma *et al.* (2019) resorted to the generation of streaks to counter transient instabilities, Yao & Hussain (2019) investigated the impact of spanwise wall oscillation on the drag of a supersonic turbulent boundary layer, and Jahanbakhshi & Zaki (2021) took advantage of the sensitivity of the Mack modes to temperature to delay transition to turbulence. More recently, Celep *et al.* (2022) combined both streak generation and wall heating/cooling effects to control oblique breakdown in a supersonic boundary layer. However, all the aforementioned studies employed predetermined active strategies that do not exploit any real-time measurement and may therefore be less cost-effective and robust to changes in operating conditions than a reactive control strategy (Gad-el Hak 2000). To the best of our knowledge, reactive control of convective instabilities in a supersonic boundary layer has not yet been considered.

Contrary to oscillator flows (Barbagallo, Sipp & Schmid 2009; Schmid & Sipp 2016), which are by definition linearly globally unstable (Huerre & Monkewitz 1990) and have intrinsic dynamics, noise-amplifier flows like the supersonic boundary layer are extremely sensitive to external disturbances, which are amplified downstream as they are convected by the flow (hence the name convective instabilities). In this context, the purpose of reactive control is to cancel out noise-induced perturbations (Bagheri, Brandt & Henningson 2009; Barbagallo *et al.* 2012) by producing destructive interferences with an actuator. This task is difficult for mainly two reasons: (a) the detection of the time delay associated with the convection of perturbations that may trigger out-of-phase actions with respect to the incoming perturbations; (b) the wide spatially evolving range of amplified frequencies along the plate, from higher frequencies upstream to lower ones downstream.

1.1. *Historical dominance of feedforward/linear–quadratic–Gaussian synthesis for the control of noise-amplifier flows*

Controller synthesis is feasible only for models of small dimensions, of the order of 10^2 degrees of freedom at most, because of the computational cost and storage requirements

of currently available tools (Ramesh, Utku & Garba 1989). Therefore, most fluidic control problems require the identification of reduced-order models (ROMs), using for instance the eigensystem realization algorithm (ERA) on impulse response data. This popular tool, introduced by Juang & Pappa (1985), has already been used in many control studies for noise-amplifier flows (Belson *et al.* 2013; Dadfar *et al.* 2013; Sasaki *et al.* 2020; and many others). Once ROMs are obtained, the control law is built with classical tools of control theory that are mathematically well-established in a linear framework and thus perfectly suited for controlling the linear growth of small perturbations.

In noise-amplifier flows, there is no synchronization of the dynamics at a global scale, and perturbations from an actuator u are rapidly damped in the upstream direction, hence the control set-up changes fundamentally depending on the position of the estimation sensor y relative to u. When y is placed upstream, actuator-induced perturbations are not observable, and the configuration is termed 'feedforward' (Bagheri *et al.* 2009; Semeraro *et al.* 2011; Hervé *et al.* 2012; Juillet, Schmid & Huerre 2013; Morra *et al.* 2020). On the other hand, when y is placed downstream, the sensor measures the superposition of noise-induced and actuator-induced perturbations, hence the term 'feedback' (Barbagallo *et al.* 2012; Belson *et al.* 2013; Semeraro *et al.* 2013*b*; Vemuri *et al.* 2018; Tol, Kotsonis & de Visser 2019). In this case, though, there may be a significant time delay before the effect of actuation may be seen by the sensor, because perturbations are convected at a finite rate by the underlying base flow: the farther downstream y is, the longer the delay.

The literature on noise-amplifier control is dominated by the linear–quadratic–Gaussian (LQG) synthesis (Semeraro *et al.* 2011; Barbagallo *et al.* 2012; Juillet *et al.* 2013; Sasaki *et al.* 2018*a*; Tol *et al.* 2019; and many others), a synthesis method dating back to the 1960s (Kalman 1964). Despite being theoretically optimal with respect to a performance criterion, this method comes with no guarantees on stability margins (Doyle 1978). In other words, tiny errors in the model may end up with an unstable feedback loop when y is placed downstream of u (feedback set-up), which represents a major drawback for practical applications. Using the loop-transfer-recovery method, it is in some cases possible to overcome this lack of stability robustness by overwhelming the control signal entering the estimator (Kwakernaak 1969; Doyle & Stein 1981). This procedure has, for example, been used successfully by Sipp & Schmid (2016) to improve the stability robustness of their controller in the case of a flow over an open square cavity (oscillator flow). The recovery procedure works by inverting the plant dynamics in order to obtain ultra-fast estimators. This procedure leads to an unstable closed loop in the case of systems with time delays, because they possess right-half-plane zeros that are converted into right-half-plane poles (Zhang & Freudenberg 1987; Skogestad & Postlethwaite 2005; Sipp & Schmid 2016). As a result, this method is not suitable for noise-amplifier flows in general, and in particular, the supersonic boundary layer flow. Contrary to the feedback structure, the feedforward design is unconditionally stable, and its implementation via LQG synthesis is not a problem. Therefore, feedforward configurations combined with LQG syntheses dominate the noise-amplifier flow control literature, particularly in the incompressible boundary layer control studies (Bagheri *et al.* 2009; Semeraro *et al.* 2011, 2013*a*,*b*; Dadfar *et al.* 2013, 2014; Sasaki *et al.* 2018*a*, 2020; Freire *et al.* 2020; Morra *et al.* 2020).

1.2. *Feedforward 'Achilles heel': performance robustness*

However, the use of a feedforward set-up raises the problem of robustness to performance, which can be defined as the control law's ability to remain efficient in terms of perturbation amplitude reduction despite modelling errors or free-stream condition variations around

the reference case. This problem has been little addressed in the boundary layer control literature, despite the advent of robust synthesis, introduced by Doyle *et al.* (1989). So far, these modern methods have been used mainly in the case of oscillator flows (Flinois & Morgans 2016; Leclercq *et al.* 2019; Shaqarin *et al.* 2021) to have some stability guarantees, because using a feedback set-up is mandatory to stabilize a globally unstable flow.

To improve performance robustness compared to a simple fixed-structure LQG feedforward controller, Erdmann *et al.* (2011) and Fabbiane *et al.* (2014, 2015) used an adaptive feedforward method for boundary layer control, based on the filtered-X least-mean-squares (FXLMS) algorithm, where the controller structure is adjusted according to the variations of the flow conditions through real-time measurements. However, this method is not robust to abrupt changes in inflow conditions because the controller coefficients are adjusted in a quasi-static fashion. Due to its natural ability to be robust to unknown disturbances or uncertainties on the model (Skogestad & Postlethwaite 2005), feedback design appears to be a promising alternative for performance robustness on short time scales. Barbagallo *et al.* (2012) employed a feedback structure combined with an LQG synthesis to control instabilities over a backward-facing step, and emphasized the importance of placing the estimation sensor close to the actuator to obtain a reasonable performance. Doing so increases the controllable bandwidth indeed, as it is limited in feedback set-up by the convection delay of the disturbances from the actuator to the estimation sensor. However, some of their feedback controllers turned out to be unstable on the real plant (the full linearized Navier–Stokes equations), because of the poor stability robustness of LQG synthesis to tiny errors in the ROM. Tol *et al.* (2019) also obtained some unstable controllers when trying to control Tollmien–Schlichting (TS) waves in an incompressible two-dimensional (2-D) boundary layer using LQG synthesis on a feedback set-up. Belson *et al.* (2013) are among the first to demonstrate the feasibility of a feedback set-up with stability and performance robustness for the same flow, using a simple proportional integral (PI) controller that was tuned by hand. However, the simple structure of the PI controller did not allow them to obtain a satisfactory performance for the chosen actuator/sensor pair, forcing the authors to change it, despite the good performance obtained with LQG synthesis on the ROMs with the same actuator/sensor pair. A similar approach was used by Vemuri *et al.* (2018) in order to cancel out TS waves in an experimental set-up. The authors tuned a proportional controller by hand to optimize the controller gain in a closed loop while ensuring robust stability of their feedback configuration. Such loop-shaping approaches provide guarantees on stability robustness but are far from optimal from a performance viewpoint. And perhaps more importantly, they are very limited in the sense that they cannot be applied to more complex controller structures in a systematic way.

1.3. *Designing robust controllers: structured mixed H_2/H_∞ synthesis techniques*

In contrast, modern tools for robust multi-criteria synthesis, such as the structured mixed H_2/H_∞ synthesis (Apkarian, Gahinet & Buhr 2014), allow us to optimize complex control laws. The structured mixed H_2/H_∞ synthesis is able to treat different kinds of mathematical criteria simultaneously, contrary to the LQG method, which minimizes a single quadratic criterion based on performance and cost. Furthermore, structured synthesis (Apkarian & Noll 2006) has the advantage of limiting the controller order and imposing its structure beforehand (e.g. state-space model of order 10, proportional integral derivative controller, etc.), unlike methods that solve Riccati equations, such as LQG (Freire *et al.* 2020), H_∞ (Flinois & Morgans 2016) or H_2 (Tol *et al.* 2017) optimal

controls, which lead to high-order controllers (of the same order as the plant augmented by weighting functions). These are often too expensive to use in real-time applications, and require reducing the controller order in a post-processing step. Performing this reduction optimally while maintaining stability and performance guarantees on the closed loop remains an open problem (Chen, Zhou & Chang 1994; Goddard & Glover 1995). The possibility of working with both H_2 (an integrated gain over all frequencies) and H_∞ (the maximum gain over all frequencies) criteria ensures performance, robustness to stability and robustness to performance (Apkarian, Noll & Rondepierre 2010). Indeed, the use of H_∞ criteria on some transfer functions allows us to respect stability margins on the feedback design (what was missing within the LQG synthesis) despite modelling errors, and to desensitize the controller on certain frequency ranges, allowing optimal performance to be maintained despite the presence of, for example, noise on the estimation sensor. The use of H_2 criteria makes it possible to have a performance objective of disturbance rejection during the synthesis (which was sometimes lacking in previous feedback studies).

1.4. *Objective and outline of the paper*

In the present paper, we will consider a supersonic boundary layer at $M = 4.5$ and focus on 2-D (i.e. spanwise-invariant) and linear perturbations. We will not be dealing with oblique modes or finite-amplitude perturbations, even if they often do play a significant role in transition in practice. Hence the present work is only a first step in learning how to design robust control laws for the problem of transition in the supersonic boundary layer. One key question that we wish to address before introducing more physical complexity is how do the feedforward and feedback set-ups compare on this noise-amplifier flow, using modern robust synthesis tools? With the help of multi-criteria structured H_2/H_∞ controller synthesis, can we design a feedback set-up that outperforms the often-used feedforward/LQG synthesis with regards to performance robustness to realistic changes in operating conditions, i.e. velocity and density variations?

The paper is organized as follows. Sections 2 and 3 provide a description of the flow configuration and numerical methods. In § 4, local and global linear stability tools are used to define appropriate closed-loop specifications, i.e. determining the actuators, sensors and performance criterion to be optimized. Section 5 is devoted to ROM identification from impulse responses using the ERA, with special emphasis on the problem of time delays in such noise-amplifier flows. Next, we formally introduce the multi-criteria structured mixed H_2/H_∞ synthesis and the associated constraint minimization problem that we wish to solve. In § 6, we compare the results obtained on and off design (noisy sensors, density and velocity variations) for the feedforward and feedback set-ups. Conclusions are drawn in § 7.

2. Flow configuration

A 2-D compressible ideal gas flowing over a flat plate is considered. The flow is governed by the Navier–Stokes equations:

$$\frac{\partial \rho}{\partial t} + \nabla \cdot (\rho \boldsymbol{u}) = 0, \tag{2.1a}$$

$$\frac{\partial \rho \boldsymbol{u}}{\partial t} + \nabla \cdot (\rho \boldsymbol{u} \otimes \boldsymbol{u}) = -\nabla p + \nabla \cdot \boldsymbol{\tau}, \tag{2.1b}$$
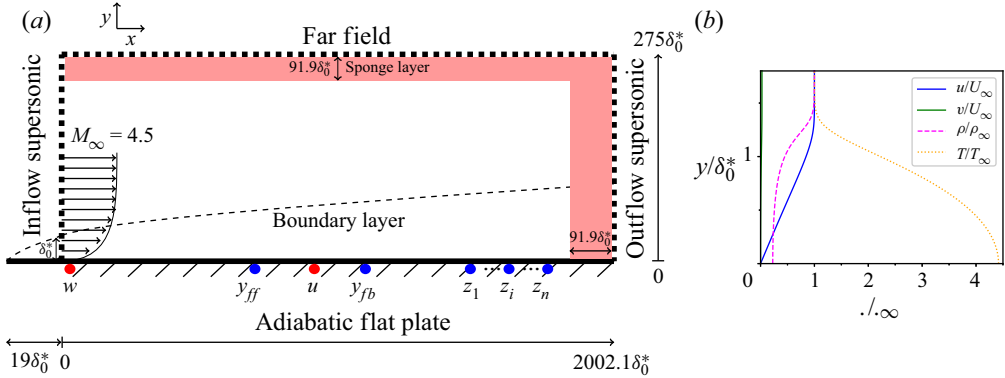
Figure 1. (*a*) Diagram of the computational domain. Inputs and outputs of the control problem are in red and blue, respectively. (*b*) Boundary layer profile used for the inlet condition.

$$\frac{\partial \rho E}{\partial t} + \nabla \cdot (\rho E \boldsymbol{u}) = \nabla \cdot (-p\boldsymbol{u} + \boldsymbol{\tau} \cdot \boldsymbol{u} - \boldsymbol{\theta}), \tag{2.1c}$$

where ρ is the fluid density, $\boldsymbol{u}$ is the velocity vector, p is the static pressure, $E = p/\rho(\gamma - 1) + (\boldsymbol{u} \cdot \boldsymbol{u})/2$ is the total energy, $\boldsymbol{\tau}$ is the viscous stress tensor, and $\boldsymbol{\theta}$ is the heat flux vector. The viscous stress tensor and the heat flux vector are given by

$$\boldsymbol{\tau} = \mu \left(\nabla \otimes \boldsymbol{u} + (\nabla \otimes \boldsymbol{u})^{\mathrm{T}} - \tfrac{2}{3}(\nabla \cdot \boldsymbol{u})\boldsymbol{I} \right), \tag{2.2}$$

$$\boldsymbol{\theta} = -k \nabla T, \tag{2.3}$$

with $\boldsymbol{I}$ the identity tensor, k the thermal conductivity, and μ the dynamic viscosity, which is deduced from the local temperature T via Sutherland's law,

$$\mu = \mu_{ref} \left(\frac{T}{T_{ref}} \right)^{3/2} \frac{T_{ref} + S}{T + S}. \tag{2.4}$$

The parameters of Sutherland's law are taken as $\mu_{ref} = 1.716 \times 10^{-5}$ Pa s, $T_{ref} = 273.15$ K and $S = 110.4$ K. The gas considered being air, we have $\gamma = 1.4$, $r = 287$ J K^{-1} kg^{-1} and $Pr = \mu \gamma r / k(\gamma - 1) = 0.725$. The free-stream flow conditions are very close to those used experimentally by Kendall (1975) and in the simulations of Ma & Zhong (2003), i.e. $T_\infty = 65.149$ K, $U_\infty = 728.191$ m s^{-1} and $p_\infty = 728.312$ Pa. Thus the free-stream Mach number of the simulation is $M_\infty = U_\infty / \sqrt{\gamma r T_\infty} = 4.5$.

The computational domain is represented in figure 1(*a*). It consists of a rectangular domain where the lower boundary is an adiabatic flat plate of length $L_x = 2002.1\delta_0^*$, with $\delta_0^* = 3.2656 \times 10^{-4}$ m the compressible displacement thickness at the inlet of the domain (defined as $\delta_0^* = \int_0^\infty (1 - \rho u / \rho_\infty u_\infty)\, \mathrm{d}y$), which results in $Re_{\delta_0^*} = \rho_\infty U_\infty \delta_0^* / \mu_\infty \approx 2121$.

Far-field and supersonic exit conditions are respectively applied at the top ($y = 275\delta_0^*$) and at the outlet of the computational domain. Furthermore, a sponge area is used downstream and in the upper part of the domain to minimize reflections. This sponge area has length $L_{sponge} = 91.9\delta_0^*$ in both streamwise and wall-normal directions; it consists in adding a source term in (2.1) on the last 10 cells closest to the boundaries to bring the flow back to its equilibrium point. In addition, the mesh is stretched in the longitudinal direction for the downstream boundary (30 cells in the streamwise direction). A supersonic inlet

954 A20-6

condition is imposed at the upstream boundary where the complete state is prescribed and matches a zero-pressure gradient laminar boundary layer profile (see figure 1*b*) computed with the ONERA boundary layer code CLICET (see, for instance, Olazabal-Loume *et al.* 2017). It corresponds to a profile taken at distance $19\delta_0^*$ from the leading edge. The beginning of the numerical domain has been chosen to be in a stable area for all frequencies according to local linear stability theory (see § 4.1). The boundary layer thickness (denoted δ) at the end of the domain of interest leads to $Re_\delta \approx 35\,081$. Overall, the useful numerical domain (i.e. not counting the length of the sponge area) extends over $4 \times 10^4 < Re_x = \rho_\infty U_\infty x / \mu_\infty < 4.1 \times 10^6$.

3. Base-flow and spatial stability analyses

3.1. *Base flow and linearized DNS*

Direct numerical simulations (DNS) are performed using the finite volume code elsA (Cambier, Heib & Plot 2013). An upwind AUSM + up scheme (Liou 2006) associated with a third-order MUSCL extrapolation method (van Leer 1979) is used for the spatial discretization of the convective fluxes. The viscous fluxes are obtained by a second-order centred scheme. The semi-discretized Navier–Stokes equations then read

$$\frac{\mathrm{d}\boldsymbol{q}}{\mathrm{d}t} = \boldsymbol{N}(\boldsymbol{q}) + \boldsymbol{P}\boldsymbol{f}, \tag{3.1}$$

where $\boldsymbol{q} = [\rho, \rho\boldsymbol{u}, \rho E]^{\mathrm{T}}$, and $\boldsymbol{N}(\boldsymbol{q})$ is the discretized compressible Navier–Stokes equations (including the boundary conditions). The momentum forcing $\boldsymbol{f}$ may represent either a noise source or the effect of an actuator. The matrix $\boldsymbol{P}$ represents the prolongation operator that transforms the momentum forcing into a full state-vector forcing by adding zero components. The laminar base flow $\bar{\boldsymbol{q}}$, defined as

$$\boldsymbol{N}(\bar{\boldsymbol{q}}) = 0, \tag{3.2}$$

is obtained by time stepping the unforced unsteady (3.1) with an implicit time-stepping method based on a local time step, up to convergence of the residuals. The unsteady simulations for the development of instabilities are performed with an implicit second-order Gear scheme (Gear 1971) with four sub-iterations and a time step dt ensuring a Courant–Friedrichs–Lewy number lower than 1.4 in the whole domain. For these unsteady simulations, the amplitude of the forcing $\boldsymbol{f}$ is chosen sufficiently small to ensure that the induced perturbation $\boldsymbol{q}' = \boldsymbol{q} - \bar{\boldsymbol{q}}$ remains in the linear regime until the end of the computational domain. The time step and the number of sub-iterations of the temporal method have been validated by comparing transfer functions from the linearized DNS and those determined from the frequency-domain resolvent approach (defined in § 3.2).

A resolution of 3200×220 cells for the useful domain is chosen. The mesh is uniform in the x direction, while a geometric law is used in the y direction to resolve strong gradients near the wall. The base-flow and linear growth rates have been verified against the linearized DNS results of Ma & Zhong (2003), allowing us to validate the resolution and the numerical schemes (see Appendix A).

3.2. *Global resolvent analysis*

For purposes of controlling instabilities, the choice of the type and position of the actuator/sensors will play an essential role. This choice is guided by resolvent analysis,

which characterizes the noise-amplifier behaviour from an input–output viewpoint. The method is detailed briefly in this subsection.

The purpose of control is to reduce the amplitude of disturbances that develop naturally in the boundary layer, and thus to maintain the flow as close as possible to its equilibrium $\bar{q}$. By injecting the ansatz $q = \bar{q} + q'$ into (3.1) and considering only small-amplitude forcing f, we obtain after linearization that

$$\frac{\mathrm{d}q'}{\mathrm{d}t} = Aq' + Pf, \tag{3.3}$$

where A is the Jacobian matrix defined as $A = \mathrm{d}N/\mathrm{d}q|_{\bar{q}}$. In our configuration, all the eigenvalues of A have a negative real part, and the flow is therefore globally stable. Switching to the frequency domain, a direct relation between the spatial structure of a harmonic forcing $f(x, y, t) = \tilde{f}(x, y)\,\mathrm{e}^{\mathrm{i}\omega t}$ and its flow response $q'(x, y, t) = \tilde{q}(x, y)\,\mathrm{e}^{\mathrm{i}\omega t}$ is established:

$$\tilde{q} = R\tilde{f}, \tag{3.4}$$

where $R = (\mathrm{i}\omega I - A)^{-1} P$ is the resolvent operator, and $\omega = 2\pi f \in \mathbb{R}$ is the angular frequency. For a given frequency and among all the possible forcings, we examine the one that maximizes the gain:

$$\tilde{g}^2(\omega) = \sup_{\tilde{f} \neq 0} \frac{\|\tilde{q}\|_E^2}{\|\tilde{f}\|_F^2}, \tag{3.5}$$

where $\| \cdot \|_E^2$ and $\| \cdot \|_F^2$ respectively denote the Chu energy norm and the energy of the momentum forcing (Bugeat *et al.* 2019). The Chu energy is defined as

$$E_{Chu} = \frac{1}{2} \int_{\mathcal{V}} \left(\overbrace{\underbrace{\bar{\rho}(|u'|^2 + |v'|^2)}_{e_{u'}} + r\,\frac{\bar{T}}{\bar{\rho}}\,\underbrace{|\rho'|^2}_{e_{\rho'}} + \underbrace{\frac{r}{\gamma - 1}\,\frac{\bar{\rho}}{\bar{T}}\,|T'|^2}_{e_{T'}}}^{e_{Chu}} \right) \mathrm{d}V; \tag{3.6}$$

it contains terms relative to thermodynamic perturbations in addition to the kinetic one, and is therefore commonly used to study the global behaviour of compressible flows (Hanifi, Schmid & Henningson 1996; Bugeat *et al.* 2019). For a given frequency, the fields $\tilde{f}$ and $\tilde{q}$ corresponding to the optimal gain $\tilde{g}$ are respectively called optimal forcing and response modes. Determining the optimal gain amounts to computing the largest eigenvalue of a positive generalized eigenvalue problem with the Arnoldi algorithm (ARPACK library, Lehoucq, Sorensen & Yang 1998) using a sparse LU solver (MUMPS library, Amestoy *et al.* 2001) for linear system solution. The Jacobian matrix $A = \mathrm{d}N/\mathrm{d}q|_{\bar{q}}$ is extracted explicitly using a second-order finite-difference method (Beneddine 2017). This global analysis tool developed in previous work (Beneddine, Mettot & Sipp 2015) was validated on the supersonic boundary layer results of Bugeat *et al.* (2019). In our study, the domains involved in the definition of $\| \cdot \|_E^2$ and $\| \cdot \|_F^2$ correspond to both $x \in [0; 1910.2\delta_0^*]$ and $y \in [0; 92\delta_0^*]$.

3.3. *Local stability analysis*

The primary aim of the local linear stability theory (LLST) for the present study is to classify the mechanisms involved in our DNS and resolvent analysis by associating local

modal mechanisms from the LLST with those observed in our purely non-modal DNS and global resolvent study. Indeed, the flow being globally stable, the growth of disturbances is due only to non-modal phenomena. These non-modal effects are a consequence of the non-normality of A (Schmid 2007). The non-normal effects can be cast in two categories for open-flows: the component-type non-normality, and the convective-type non-normality (Sipp *et al.* 2010). Component-type non-normality is characterized by a componentwise transfer of energy between the forcing and response fields, like in the Orr or lift-up mechanisms (Bugeat *et al.* 2019) – but note that the latter is absent here since lift-up is three-dimensional (3-D). Convective-type non-normality is caused by modal amplification on the local scale and is characterized by a separation of the spatial supports of the forcing and response fields.

In LLST, we consider perturbations that are evolving very rapidly in the x direction compared to the base flow. At each streamwise position, the base flow is considered frozen with respect to the perturbations $\phi' = [\rho', u', v', T']$, therefore the latter can be sought in the form

$$\phi' = \tilde{\phi}(y)\,\mathrm{e}^{\mathrm{i}(\alpha x - \omega t)}, \tag{3.7}$$

where in general the wavenumber α and the frequency ω are complex numbers. Plugging this ansatz into the linearized Navier–Stokes equations with frozen base-flow profile leads to a different dispersion relation $D(\alpha, \omega; x) = 0$ for each value of x. In the spatial stability framework, we consider real angular frequencies ω and solve for the complex wavenumber $\alpha = \alpha_r + \mathrm{i}\alpha_i$, where α_r is the wavenumber, and $-\alpha_i$ is the spatial growth rate along x. All perturbations are assumed to vanish at the free-stream boundary $y \to \infty$, while on the flat plate, $y = 0$, $\tilde{u} = \tilde{v} = 0$ and $\mathrm{d}\tilde{\rho}/\mathrm{d}y = \mathrm{d}\tilde{T}/\mathrm{d}y = 0$ (adiabatic plate). Equations are discretized along the wall-normal direction y using a Chebyshev collocation method. For all values of x and ω, an eigenvalue problem is solved, using the LAPACK library, in order to determine the complex eigenvalue α and corresponding eigenvector $\tilde{\phi} = [\tilde{\rho}, \tilde{u}, \tilde{v}, \tilde{T}]$. The analysis is performed using an in-house code detailed fully in Saint-James (2020) and validated here by comparing with the linear local growth rates of the supersonic boundary layer from Ma & Zhong (2003).

4. Noise-amplifier behaviour and control set-up

4.1. *Characterization of instabilities*

The local spatial stability diagram of spanwise-invariant perturbations is displayed in figure 2(a), with $F = 2\pi f \delta_0^*/U_\infty$ the dimensionless frequency. It is characterized by two distinct instability regions (i.e. where the spatial growth rate is positive, $-\alpha_i > 0$): one for the first Mack mode, and one for the second Mack mode. For each mode, the instability domain (depicted by the red solid line) for a given frequency is located between branch I (convectively stable/unstable boundary) and branch II (convectively unstable/stable boundary). Each frequency is therefore amplified only on a certain portion of the domain: high frequencies are amplified upstream, while low frequencies are found further downstream. Compared to the first mode, the unstable frequencies of the second mode are higher and are associated with higher growth rates. Transition to turbulence is often predicted from LLST using the N-factor (Smith & Gamberoni 1956)

$$N(\omega, x) = \int_{x_c}^{x} -\alpha_i(\omega)\,\mathrm{d}x = \ln\left(\frac{|\phi'|}{|\phi'|_c}\right), \tag{4.1}$$
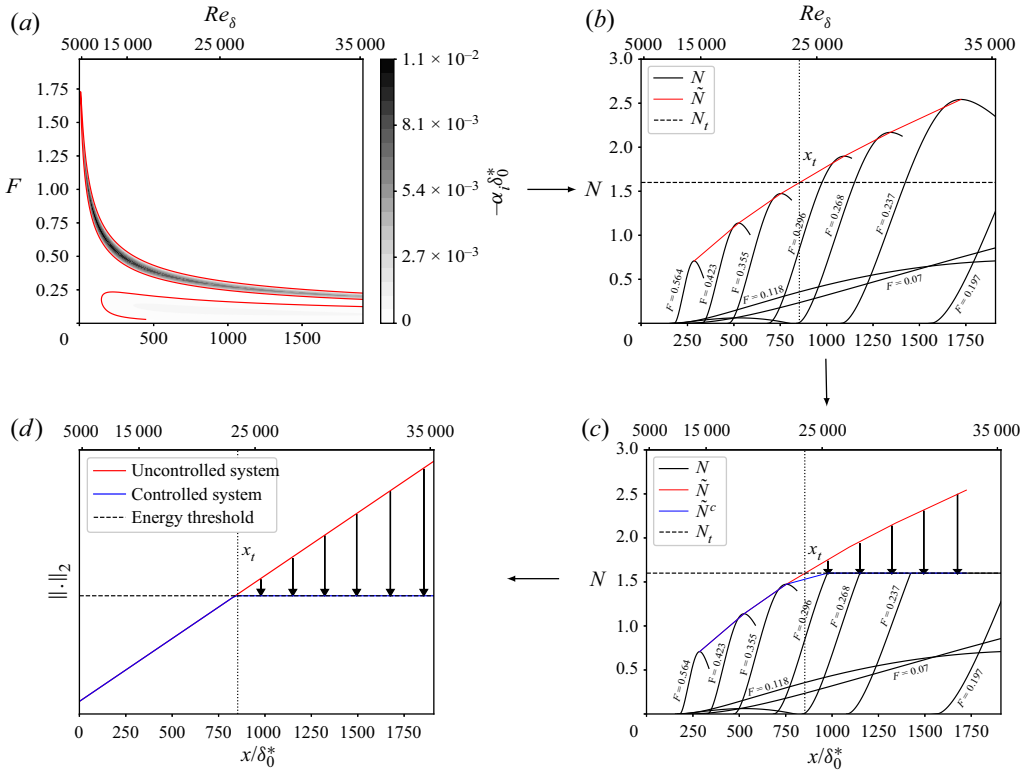
Figure 2. (*a*) Stability diagram; red solid lines represent isolines $\alpha_i = 0$. (*b*) Calculation of the N-factors (black solid lines) for transition prediction based on LLST: transition occurs at x_t when $\tilde{N} > N_t$ (notional diagram). (*c*) Performance objective for closed-loop control based on the N-factor criterion. (*d*) Modification of the N-factor criterion using the H_2 norm, in order to reduce conservatism. The quantity $F = 2\pi f \delta_0^*/U_\infty$ represents the dimensionless frequency.

with x_c the location of branch I for the considered frequency, and $|\phi'|_c$ the amplitude of the mode at this location. The N-factors for different frequencies are represented in figure 2(*b*). Although the instability range of the first Mack mode is larger, the N-factors of the second mode are greater all along the domain due to their higher growth rates. Transition is often assumed to occur when the quantity $\tilde{N}(x) = \max_\omega N(\omega, x)$ (red solid lines in figures 2*b,c*) at the position x_t reaches a threshold value N_t (dashed lines in figures 2*b,c*, placed arbitrarily for the explanation). This criterion means that the transition process begins when a perturbation has been amplified by a factor e^{N_t}. Thus in order to delay transition to turbulence, when $x > x_t$, a control action should transform the quantity $\tilde{N}$ obtained without control into the quantity $\tilde{N}^c$ (blue line in figure 2*d*) with control, such that $\tilde{N}^c < N_t$ for as long as possible (see figure 2*d*). The dominant frequency being different at each streamwise location of the domain, a large frequency range needs to be controlled, which complicates the design of the control law. The $\tilde{N}^c < N_t$ criterion could be translated directly into an H_∞ criterion, because this would mean that the maximum amplification over the entire frequency spectrum must not exceed a threshold over the entire domain, exactly as in the N-factor method. However, this method may be considered conservative as it is based on the worst perturbation, which is purely harmonic and therefore not quite realistic (Mack 1977). Fedorov & Tumin (2022) recommended instead the use of a criterion

954 A20-10

based on both the N-factors and the entire frequency spectrum of the incoming disturbance $|\phi'|_c$, which amounts to considering an H_2 norm rather than an H_∞ norm. We follow this recommendation and choose a performance objective based on an H_2 norm. More precisely, our objective will be to maintain the spatially integrated amplification below a given threshold along the plate, and this integrated amplification will be quantified using an H_2 norm (see figure 2d).

The global stability results based on resolvent analysis complement those obtained previously from LLST. The optimal energy gain $\tilde{g}$ as a function of the forcing frequency F is represented in figure 3(a). This curve displays two peaks at $F \approx 0.118$ and $F \approx 0.237$, which correspond respectively to the first and second Mack modes identified in LLST. Global resolvent analyses are consistent with those of the local approach, since the optimal energy gain is closely related to N-factors (Sipp *et al.* 2010; Beneddine *et al.* 2015).

For the frequency $F = 0.237$ leading to the highest gain, the real parts of the streamwise optimal forcing and velocity response are shown in figures 3(b,c). The spatial structure of the forcing is located upstream of the domain, while that of the response is located further downstream. This separation of the spatial supports, related to the convective-type non-normality of the Jacobian operator, implies a time delay between actuation upstream and sensing downstream, making the design of a robust control law even more complex.

Figure 3(d) shows that the peak of the forcing density $d_{e_f}(x) = \int_0^{y=92\delta_0^*} \|\tilde{f}\|^2 \, \mathrm{d}y$ (resp. Chu energy density $d_{e_{Chu}}(x) = \int_0^{y=92\delta_0^*} e_{Chu} \, \mathrm{d}y$) is not very far from the position of branch I (resp. II) from LLST (Sipp *et al.* 2010). The energy of the response is dominated at each abscissa by the thermodynamic quantities $e_{T'}$ and $e_{\rho'}$, while quantity $e_{u'}$ has a smaller contribution. Note that the most amplified frequencies depend on the extent of the domain used in the optimization problem (not shown here): the longer the domain, the lower the dominant frequency. The gain of the frequencies that already reach their peak of forcing density and Chu energy density (linked to the positions of branches I and II, respectively) does not vary with an increase of the domain size in the streamwise direction as these frequencies can no longer be amplified. For all the other frequencies (which are lower), the phenomenon of amplification continues, leading to higher gains for a wider area.

A comparison between the spatial amplification rates $-\alpha_i$ from LLST (red dashed line) and $-\tilde{\alpha}_i = (1/|\tilde{u}(x, y = 1.7\delta_0^*)|)\partial_x|\tilde{u}(x, y = 1.7\delta_0^*)|$ from resolvent analysis (black dashed line) is depicted in figure 3(e). The quantity $-\tilde{\alpha}_i$ represents the slope of $\ln|\tilde{u}|$ with respect to x (black solid line) and can therefore be compared to a growth rate; when the convective-type non-normality effects dominate, this growth rate is independent of the choice of y and the primitive variable. The growth of the resolvent mode within $x \in [0; 1078\delta_0^*]$ is due to the optimal forcing that is non-zero in this region (see figure 3d) and that induces the response. The inclined pattern in the forcing field (see figure 2b) indicates that the response also takes advantage of the Orr mechanism (Orr 1907) and more generally of non-modal local interactions. After this initial growth region induced by the forcing, both $-\alpha_i$ and $-\tilde{\alpha}_i$ exhibit similar values in the region in $x \in [1200\delta_0^*; 1730\delta_0^*]$, which indicates that transient growth is then dominated by the convective instability associated with the second Mack mode.

To maximize the amplification of the second Mack mode, the forcing field (see figures 3b,f) must be localized near the generalized inflection point y_g (denoted in figures 3b,c,f,g with a dashed line), defined as $\partial_y(\bar{\rho}\,\partial_y\bar{u})|_{y_g} = 0$. A region of supersonic instabilities (below the dashed-dotted line in figures 3b,c,f,g) – defined as $\hat{M} = |\bar{u} - \omega/\tilde{\alpha}_r|/\sqrt{\gamma r \bar{T}} > 1$, with $\tilde{\alpha}_r$ the global resolvent streamwise wavenumber computed
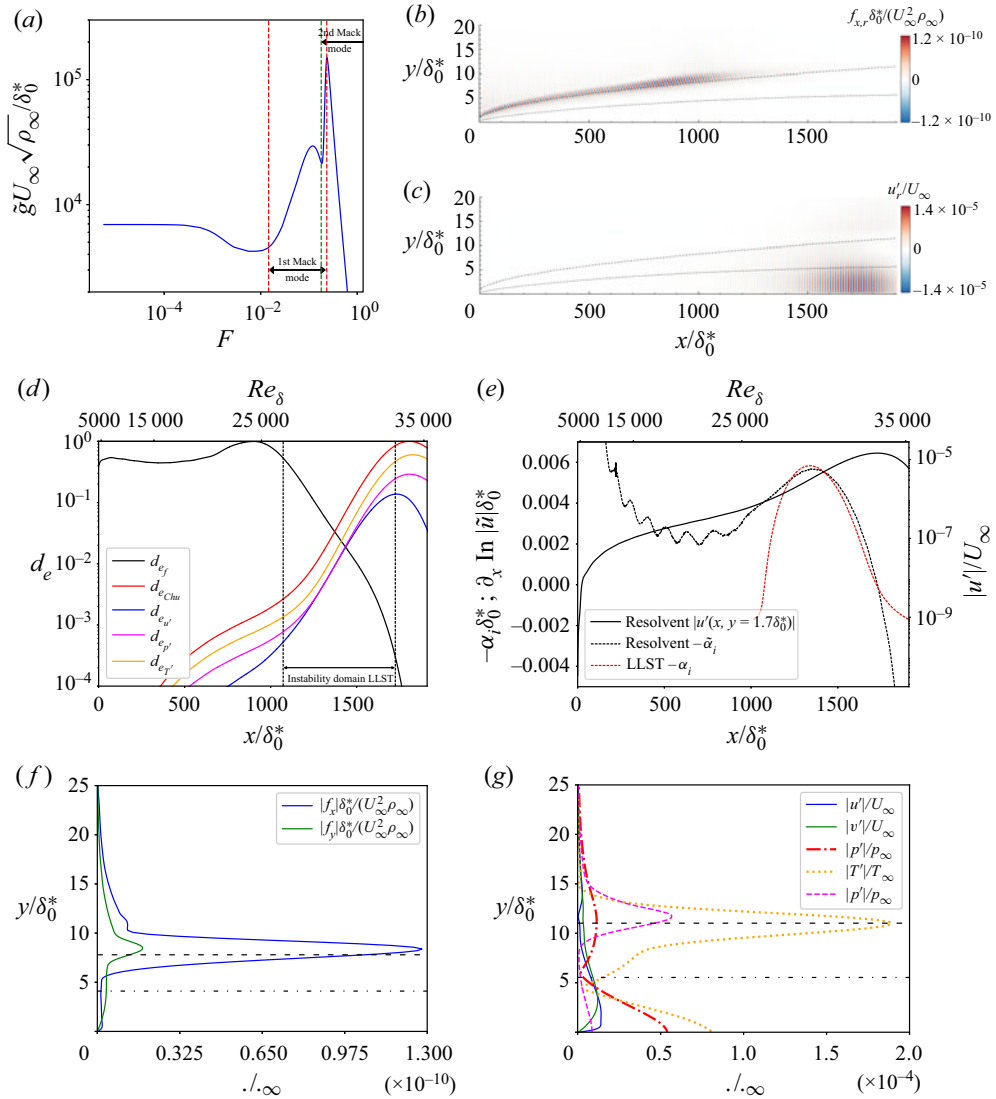
Figure 3. (*a*) Optimal resolvent gain as a function of the dimensionless frequency F. According to LLST, red and green dashed areas represent the unstable frequency range of first and second Mack modes, respectively. The region where both modes are unstable corresponds to an area where the first mode is unstable over a tiny distance. (*b*) Real part of the streamwise component of the optimal forcing and (*c*) its associated streamwise velocity response, at $F = 0.237$. (*d*) Evolution at $F = 0.237$ of the forcing density and the different contributions to the Chu energy density normalized by their maximum values. The positions of branches I and II from LLST are symbolized by vertical dashed lines. (*e*) Comparison of $-\alpha_i$ and $-\tilde{\alpha}_i$ at $F = 0.237$. (*f*) Profiles of the optimal forcing components at $x = 867.2\delta_0^*$, and (*g*) response at $x = 1766.7\delta_0^*$, at $F = 0.237$. The black dashed and dashed-dotted lines in (*b*), (*c*), (*f*) and (*g*) represent respectively the generalized inflection point position and the limit of the region of supersonic instabilities ($\hat{M} > 1$ below this line).

as $\tilde{\alpha}_r = \partial_x \arg(\tilde{u})$, where arg denotes the argument of a complex number (see Beneddine *et al.* 2015) – is detected close to the wall (see figure 3*c*). This confirms that the optimal response mode at $F = 0.237$ corresponds to a second Mack mode (Mack 1984). Note that the critical layer, where $\bar{u} = \omega/\tilde{\alpha}_r$, is not shown here as it is similar to the generalized
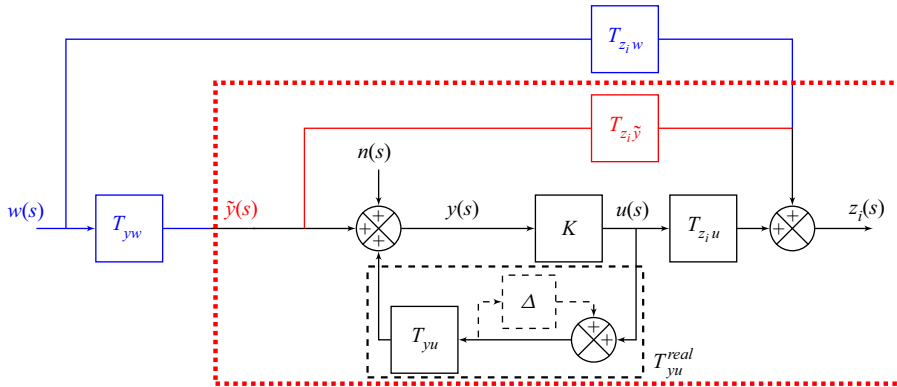
954 A20-12

Figure 4. Block diagram for noise-amplifier flows for feedforward and feedback configurations in an ideal case (with quantities in blue and black) and in a realistic set-up (with quantities in red and black). The quantities in black are common to the ideal and realistic cases. The red dotted zone therefore represents the system used with the aim of an experimentally feasible synthesis. In a feedforward set-up, $T_{yu} = \Delta = 0$.

inflection point; indeed, the phase velocity of an inflectional neutral wave in the LLST is equal to the mean velocity at y_g (Mack 1984).

Finally, we observe in figure 3(*g*) that the different components of the second Mack mode peak at different locations in the wall-normal direction y. Hydrodynamic perturbations (velocity and pressure) peak close to the wall and seem trapped in the region $\hat{M} > 1$, whereas thermodynamic quantities (density and temperature) peak near the generalized inflection point. This observation is in complete agreement with the qualitative results of Bugeat *et al.* (2019).

4.2. *Control set-up*

External perturbations are modelled using a random time signal w (see figure 1*a*) that multiplies a time-independent volume force field. In the case of small-amplitude noise considered in this paper, the dynamics is linear and will take advantage of the various instability mechanisms described in the previous subsection. If we consider several performance sensors z_i measuring the flow perturbations along the plate, then the transfer functions $T_{z_iw} = z_i(s)/w(s)$, with $s \in \mathbb{C}$ the Laplace variable, provide an accurate prediction of the downstream perturbation level without control. The reactive control set-up is depicted in figure 4. An upstream actuation u generates small-amplitude perturbations that again take advantage of the instability mechanisms to grow and eventually cancel the fluctuations at the downstream measurements z_i. The phase of the generated perturbations is therefore important and needs to be tuned with respect to the incoming perturbations that are governed by w. For this, we introduce an upstream sensor y and design a controller K, which actually corresponds to the transfer function $K = T_{uy}$, and which transforms the noise measurement y into an actuation signal u. It is straightforward to show that in the presence of control, the transfer functions from w to z_i, denoted with the superscript c, become

$$T_{z_iw}^c = T_{z_iw} + T_{z_iu}K(1 - T_{yu}K)^{-1}T_{yw}. \tag{4.2}$$

The design of K therefore requires additional transfer functions: T_{yw} characterizes the influence of noise on the upstream measurement y, T_{z_iu} characterizes the influence of the actuator on the downstream performance sensors, and for feedback set-ups only, T_{yu}

characterizes the influence of the actuator on the upstream sensor. In the following, we will assume that w is a white-noise input and will seek to reduce the expected power of the measurements z_i. This expected power, normalized by the intensity of the white-noise input, is measured by the H_2 norm of $T^c_{z_i w}$. For any stable SISO transfer function G, the H_2 norm is defined as

$$\|G\|_2 = \left(\frac{1}{2\pi} \int_{-\infty}^{+\infty} |G|^2 \, d\omega\right)^{1/2}. \tag{4.3}$$

However, determining the transfers coming from the noise w is not possible in realistic cases because the noise environment is unknown (it depends on the characteristics of the wind tunnel or the free-stream turbulence on aeroplanes). An experimentally feasible control design must therefore not be based on $T_{z_i w}$ and T_{yw}. Following Hervé *et al.* (2012), the solution proposed here is to introduce an artificial transfer function $T_{z_i \tilde{y}}$, which is intended to predict the downstream measurements z_i from the upstream measurement y in the absence of a control. This apparent transfer function (y is not a source) is defined as $T_{z_i \tilde{y}} = T_{z_i w} T_{yw}^{-1}$ (Sasaki *et al.* 2018*a,b*). In real applications, we can identify this transfer function from uncontrolled (y, z_i) data. In the following, we will consider $\tilde{y} = T_{yw} w$ as the new exogenous input of the system. We are therefore led to the modified block diagram framed by the red dotted zone in figure 4, where in case of actuation, the upstream measurement reads $y = \tilde{y} + T_{yu} u$ ($+n$, which is a measurement noise). In such a case, the controlled transfer function becomes

$$T^c_{z_i \tilde{y}} = T_{z_i \tilde{y}} + T_{z_i u} K (1 - T_{yu} K)^{-1}. \tag{4.4}$$

The ideal and realistic control schemes shown in figure 4 are related through

$$\|T^c_{z_i w}\|_2 = \| |T_{yw}| T^c_{z_i \tilde{y}}\|_2. \tag{4.5}$$

The term $|T_{yw}|$ can be replaced by the weighting function W_y whose module corresponds to $\sqrt{PSD_y(\omega)}$ (where PSD_y is the power spectral density of the estimation sensor y in the absence of control) without any loss of generality because the linear minimization problem is defined to within one amplitude; the term W_y represents the fact that the new system input $\tilde{y}$ is no longer a white noise as w but a coloured noise. Therefore, the four quantities needed for the synthesis are $T_{z_i u}$, T_{yu}, $T_{z_i \tilde{y}}$ and W_y. They can all be obtained in a realistic set-up as the temporal data of z_i, u and y would be available, and these transfers will be the ones used for identification (see § 5.1) and controller synthesis (see § 5.2). For the sake of clarity and to simplify notations, the quantity $\|W_y T^c_{z_i \tilde{y}}\|_2$ will be replaced in the rest of the paper by $\|T^c_{z_i w}\|_2$.

Maintaining closed-loop performance in spite of modelling errors or inflow conditions variations around the nominal case requires first and foremost the stability robustness of the control law. From a control design point of view, this implies considering uncertainties Δ representing a model error on T_{yu} that can lead to the instability of the feedback loop. For example, for the block Δ represented in figure 4, if no upstream noise is considered, then we have $y = (T_{yu}/(1 - \Delta))u$, so that Δ represents an inverse multiplicative uncertainty on T_{yu} such that $\Delta = (T_{yu}^{real} - T_{yu})/T_{yu}^{real}$, with T_{yu}^{real} representing the real transfer function and not the modelled one. This type of uncertainty has the advantage of representing a relative error, which facilitates its interpretation. Since $-T_{yu}^{real}K$ does not exhibit any unstable pole (T_{yu}^{real} is stable because the boundary layer flow is globally stable, while K is stable by design), the closed loop system is stable if and only if the Nyquist plot of $-T_{yu}^{real}K$ does not encircle the critical point $(-1, 0)$, which is equivalent to

$|1 - T_{yu}K|^{-1} < 1/|\Delta|$ (Skogestad & Postlethwaite 2005). Therefore, the stability of the closed loop can be guaranteed by working on the sensitivity function

$$S = (1 - T_{yu}K)^{-1}. \tag{4.6}$$

Defining the H_∞ norm of a stable SISO transfer function G as

$$\|G(s)\|_\infty = \sup_{\omega \in \mathbb{R}} |G(i\omega)|, \tag{4.7}$$

we request to maintain the H_∞ norm of the sensitivity function S below a threshold, which allows us to keep adequate stability margins. By measuring directly the minimal distance between the Nyquist plot and the critical point $(-1, 0)$ after which the closed loop becomes unstable for a negative feedback loop, the modulus margin $\|S\|_\infty^{-1}$ appears to be the most generic measure for quantifying the available stability margin (Skogestad & Postlethwaite 2005).

Finally, maintaining optimal performance despite uncertainties on a certain frequency range of the measurement y means minimizing the H_∞ norm of the transfer function

$$\frac{u}{n} = KS. \tag{4.8}$$

Desensitizing the control output u on certain frequency ranges allows us to be robust to noise n on the estimation sensor y. Even if these frequencies are attenuated far downstream of the actuator (if they are convectively stable, resulting in low $|T_{z_i \bar{y}}|$), strong injection of energy may occur in the direct vicinity of the actuator, which may in turn provoke transition to turbulence in a 3-D set-up.

In summary, the fluidic specifications for noise-amplifier flows may be reformulated from a control point of view as an optimization problem based on H_2 and H_∞ norms, in order to guarantee both performance and robustness. The constrained minimization problem for our specific study will be formulated in § 5.2.

4.3. *Selecting actuator and sensors*

For a given external perturbation, the choice of appropriate actuator and sensors is essential to ensure effective flow control. The input perturbation, representing an external disturbance (acoustic noise, roughness, free-stream turbulence, etc.) is modelled by a volume forcing $w(t) \, \boldsymbol{B}_w(x, y)$ in the right-hand side of the momentum equations (2.1b), where the noise $w(t)$ is chosen Gaussian white (with a variance sufficiently small for the perturbation to remain in the linear regime) and $\boldsymbol{B}_w(x, y)$ is divergence-free and compact in space (Bagheri *et al.* 2009; Semeraro *et al.* 2011; Belson *et al.* 2013):

$$\boldsymbol{B}_w = \boldsymbol{h} \left(\frac{10.66}{\delta_0^{*2}}, 4.1\delta_0^*, \delta_0^*, 1.5\delta_0^*, 0.15\delta_0^* \right), \tag{4.9}$$

with

$$\boldsymbol{h}(A_h, x_0, y_0, \sigma_x, \sigma_y) = A_h \begin{pmatrix} (y - y_0)\sigma_x/\sigma_y \\ -(x - x_0)\sigma_y/\sigma_x \end{pmatrix} \exp\left(-((x - x_0)/\sigma_x)^2 - ((y - y_0)/\sigma_y)^2 \right). \tag{4.10}$$

It is centred around the generalized inflection point in the wall-normal direction in order to maximize the receptivity process by exciting the optimal mechanisms of the second Mack
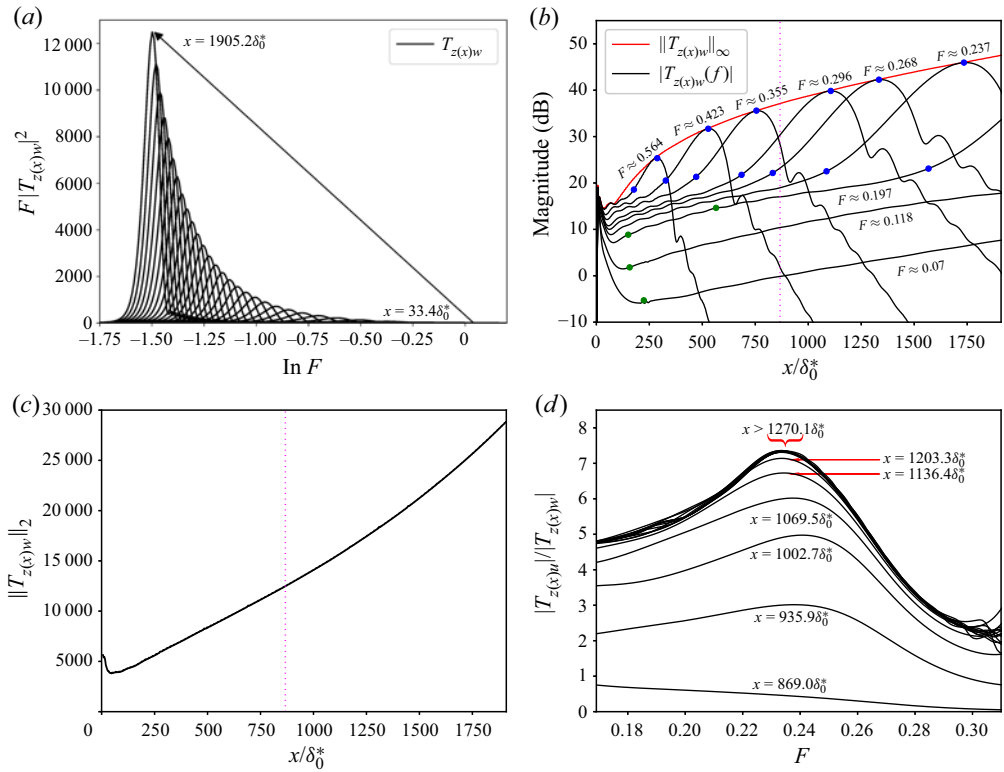
Figure 5. (*a*) Evolution of $F|T_{z(x)w}|^2$. (*b*) Variation of the frequency magnitude as a function of the plate abscissa. For each frequency, the green (resp. blue) dots represent branch I and branch II of the first (resp. second) Mack modes according to LLST. (*c*) Evolution of the H_2 norm. The vertical dotted line in (*b*) and (*c*) shows the streamwise location of the actuator $\boldsymbol{B}_u$, denoted x_u. (*d*) Evolution of the ratio $|T_{z(x)u}|/|T_{z(x)w}|$ as a function of frequency F for several plate abscissa.

mode, which is the most amplified, as shown by the resolvent analysis results in §4.1. The position of $\boldsymbol{B}_w$ in the streamwise direction is upstream of branch I (locally stable regions) for all frequencies according to the LLST.

For the sensors, in order to have strong observability of the disturbances, we choose y and $z(x)$ to be wall-pressure fluctuation sensors. This choice is supported by the fact that second Mack modes exhibit strong pressure fluctuations close to the wall, as shown by the optimal response profiles in figure 3(*g*). Also, that kind of sensor is commonly used in supersonic experimental studies (Lugrin *et al.* 2022).

In figure 5(*a*), we represent the quantity $F|T_{z(x)w}|^2$ as a function of $\ln F$, where F is the frequency, such that the integral represents the H_2 norm of $T_{z(x)w}$. The module of $|T_{z(x)w}|$ is obtained by Fourier transform of the signals from an impulse response. At each abscissa x of the plate, the energy contribution to the sensor $z(x)$ is due to only a certain frequency range. Indeed, after reaching a peak, the magnitude associated with a frequency decreases rapidly, as can be seen in figure 5(*b*). Therefore, for control, we will need to use several performance sensors z_i to obtain a suitable frequency representation at different streamwise positions, and capture the entire amplified bandwidth. As the spectrum of $F|T_{z(x)w}|^2$ is narrow (especially downstream of the domain), reducing $\|T_{z_iw}^c\|_2$ should also lead to a significant reduction in $\|T_{z_iw}^c\|_\infty$. Sufficiently far downstream from $\boldsymbol{B}_w$,

954 A20-16

the most amplified frequency at each abscissa of the domain (red line in figure 5*b*) is similar to the one that could be found with the *N*-factors (see figure 2*b*). As the magnitude of the perturbations increases for all frequencies in spatially stable regions upstream of branch I (see first dot symbols in figure 5), the perturbations seem to be subject first to a growth due to the non-modal Orr mechanism, before being dominated by the 'modal' growth of the unstable Mack mode. The highest value of $|T_{z(x)w}|$ is found at the end of the domain of interest, at frequency $F = 0.223$, close to the frequency leading to the highest gain in the global resolvent analysis ($F = 0.237$). Therefore, the optimal response mechanisms already observed in § 4.1 are well triggered by the chosen disturbance $\boldsymbol{B}_w$, which is therefore representative of a more general transition scenario due to the second Mack mode.

The control goal is to create a destructive interference by generating a second wave of appropriate amplitude and phase, which will oppose the one generated by the upstream noise $w(t)$ (Hervé *et al.* 2012; Sasaki *et al.* 2018*a*). Thus, in order to maximize the impact of control, the perturbations generated by the actuator must match those induced by the upstream noise. The incoming disturbance being mainly due to second Mack mode instabilities, an efficient actuator can be obtained with a volume forcing around the generalized inflection point in the wall-normal direction. This wall-normal actuator location is potentially far from a real experiment implementation, but the modelling of a realistic actuator is beyond the scope of our study. We just select this wall-normal position to ease the control of the instabilities by maximizing the receptivity process. We therefore consider $\boldsymbol{B}_u u(t)$ in the right-hand side of (2.1*b*) to model the actuator, with the same divergence-free spatial support as for the disturbance $\boldsymbol{B}_w$:

$$\boldsymbol{B}_u = \boldsymbol{h} \left(\frac{10.66}{\delta_0^{*2}}, 867.2\delta_0^*, 7.79\delta_0^*, 1.5\delta_0^*, 0.5\delta_0^* \right). \tag{4.11}$$

The actuator is placed sufficiently far downstream of $\boldsymbol{B}_w$ ($x_u = 867.2\delta_0^*$) for two reasons. The first is to allow disturbances to strengthen sufficiently (see figure 5*c*) to be detected easily by the estimation sensor *y* (which is close to the actuator), which in an experimental configuration would mean placing the actuator a little upstream of the beginning of the transition process. The second reason is to limit the bandwidth of the frequencies to be controlled (see figure 5*b*) in order to keep the complexity of the control problem reasonable. Hence, for the chosen streamwise position of the actuator, the frequency range to be controlled is around $F \in [0.225, 0.324]$; a more upstream actuator should have controlled a wider bandwidth. The streamwise position of the actuator remains sufficiently upstream so that incoming perturbations are controlled over a sufficiently long domain ($\sim$0.34 m) representative of an experimental configuration (the plate of the experimental tests of Kendall (1975) measured 0.35 m).

A comparison of $|T_{z(x)w}|$ and $|T_{z(x)u}|$ is shown in figure 5(*d*). It can be noted that in the vicinity of the actuator, the ratio $|T_{z(x)w}|/|T_{z(x)u}|$ evolves with the *x* abscissa. As this phenomenon no longer appears for abscissas further away from the actuator, and the ratio becomes constant, it could be attributed to a non-modal transient behaviour. Indeed, we have

$$\frac{|T_{z(x)u}|}{|T_{z(x)w}|} \propto \frac{e^{\int_{x_u}^x -(\tilde{\alpha}_i)_u \, dx}}{e^{\int_{x_u}^x -(\tilde{\alpha}_i)_w \, dx}}, \tag{4.12}$$

where $-(\widetilde{\alpha}_i)_u$ and $-(\widetilde{\alpha}_i)_w$ represent the slopes of $\ln |T_{z(x)u}|$ and $\ln |T_{z(x)w}|$ with respect to *x*, respectively. Therefore, a constant ratio implies having the same slope from a certain

	B_w	B_u	y	z_i
Streamwise position	$x_w = 4.1\delta_0^*$	$x_u = 867.2\delta_0^*$	$x_{ff} = 801.2\delta_0^*$	$x_1 = 933.2\delta_0^*$
			$x_{fb} = 885.7\delta_0^*$	$x_2 = 1029.4\delta_0^*$
				$x_3 = 1125.6\delta_0^*$
				$x_4 = 1317.9\delta_0^*$
				$x_5 = 1510.2\delta_0^*$
				$x_6 = 1766.7\delta_0^*$

Table 1. Streamwise positions of the input perturbation, the actuator and the sensors used for the identification and synthesis steps. The positions of the estimation sensor for feedforward and feedback configurations are denoted x_{ff} and x_{fb}, respectively.

distance x. This distance x represents the non-modal distance due to the receptivity of multiple modes to the volume forcing of the actuator on the flow.

The impact of the position of the estimation sensor y has already been studied extensively in the noise-amplifier flow control literature (Barbagallo *et al.* 2012; Belson *et al.* 2013; Juillet *et al.* 2013; Freire *et al.* 2020), hence the detailed analysis for the case of the supersonic boundary layer is left to Appendix B. It is just pointed out that for a feedback design, the estimation sensor y has to be close enough to the actuator to avoid sending outdated information and limit the effective delay impacting the maximum achievable performance. For a feedforward design where the impact of the actuator on the estimation sensor y is assumed to be negligible in the synthesis step ($T_{yu} = 0$), the estimation sensor has to be located sufficiently upstream of the actuator for the hypothesis to be valid.

Regarding the number of performance sensors z_i used in the identification/synthesis step, it was found by numerical simulations that six probes are required to achieve nearly uniform performance along the domain because of the need to capture the entire amplified bandwidth and the non-modal effects due to the actuator (see Appendix C). The streamwise positions of the input perturbation, the actuator and the sensors used for the identification and synthesis steps are summarized in table 1.

5. Identification and synthesis methods

5.1. *Identification of a state-space model*

Most synthesis methods require the use of state-space ROMs corresponding to the transfers involved in the controller synthesis. For the model reduction step, some of the input/output delays linked to the convective nature of the flow may be discarded due to the fact that the H_2 norm is not modified by delays. In a feedback configuration (u, y, z_i), the delays verify $\tau_{z_iu} = \tau_{z_i\tilde{y}} + \tau_{yu}$, so that

$$\|T_{z_iw}^c\|_2 = \|\mathrm{e}^{-\tau_{z_i\tilde{y}}s}W_y(T'_{z_i\tilde{y}} + \mathrm{e}^{-\tau_{yu}s}T'_{z_iu}KS)\|_2$$
$$= \| W_y(T'_{z_i\tilde{y}} + \mathrm{e}^{-\tau_{yu}s}T'_{z_iu}KS)\|_2, \tag{5.1}$$

where $T'(s)$ designates the 'dead-time-free' transfer function associated with $T(s)$. The same idea can be applied also to a feedforward design (y, u, z_i), with the result

$$\|T_{z_iw}^c\|_2 = \|W_y(\mathrm{e}^{-\tau_{uy}s}T'_{z_i\tilde{y}} + T'_{z_iu}K)\|_2. \tag{5.2}$$

Thus the only remaining delay is the one between the actuator and the estimation sensor, τ_{yu} or τ_{uy}, which is reasonably small (compared to the delays involving z_i). Removing unnecessary delays (for example, $\tau_{z_i\tilde{y}}$ in the feedback case) leads to a significant reduction in the size of the ROMs when the dead time scale is important compared to the time scale of the physical phenomenon to be captured (the period of the second Mack mode). This reduction in the order of the ROMs is beneficial for both the identification and the synthesis step: the higher the order, the more difficult the identification, and the larger the cost of the controller synthesis.

The quantities required for the synthesis are obtained by impulse responses of w and u. The state-space ROMs associated with the transfer functions $T_{z_i u}$, T_{yu} and $T_{z_i\tilde{y}}$ are obtained by the subspace identification method ERA, which requires impulse responses for each of the inputs, and involves performing a singular value decomposition to compress the state (Juang & Pappa 1985). This method has been used several times for the control of 2-D (Belson *et al.* 2013) or 3-D (Sasaki *et al.* 2018*a*; Morra *et al.* 2020) incompressible boundary layers. The ERA is applied after removing (just by shifting the time axis) either $\tau_{z_i\tilde{y}}$ (in the feedback case) or $\tau_{z_i u}$ (in the feedforward case) within the impulses from y and u to z_i. The impulse responses from y to z_i are obtained by inverse Fourier transform of $T_{z_i w}T_{yw}^{-1}$, each individual transfer function being obtained by Fourier transform of an impulse from w. The sampling time for the ERA is $5 \times dt$; the discrete time models obtained are then converted to continuous time models by the first-order hold method (Franklin, Powell & Workman 1997). As shown in figures 6(*a–c*) for the performance sensor z_6 and the feedback estimation sensor y_{fb}, the constructed ROMs capture most of the dynamics.

The identification of the quantity W_y is obtained by a vector-fitting method (Matlab function tfest) designed to fit frequency response measurements (Drmac, Gugercin & Beattie 2015). For this quantity, there is no uniqueness of the identified model as the phase can vary from one model to another without impacting the results of the synthesis (see (4.5)); the ROM just needs to be stable and causal. Hence we simply choose to define W_y such that its module fits with $\sqrt{PSD_y(\omega)}$, where y is the response from an impulse in w. Good agreement is achieved between $W_{y_{fb}}$ and the ROM in the case of the feedback estimation sensor y_{fb} (see figure 6*d*).

For the current application and with the six performance sensors z_i, the sum of the orders of each ROM is 130 for the case of the feedback configuration, and 115 for the feedforward one. By comparison, identifying the single transfer function $T_{z_6 u}$ (corresponding to the farthest performance sensor downstream) without suppressing the dead time leads to a ROM of order 220, which is already greater than the sum of the orders of each ROM without their unnecessary dead times.

In the control result in § 6, because the models are of excellent quality (see figure 6), the distinction between ROMs and real transfer functions is not deemed necessary and the depicted results are those on the complete system after implementation of the controllers in the CFD solver elsA.

5.2. *Multi-objective structured H_2/H_∞ synthesis*

In this study, control laws are designed following a structured mixed H_2/H_∞ synthesis implemented in the Matlab function systune (Apkarian *et al.* 2014). The general framework of this modern synthesis is illustrated in figure 7. In this figure, w_{H_∞} (resp. w_{H_2}) and z_{H_∞} (resp. z_{H_2}) represent the sets of inputs and outputs whose associated transfers are subject to H_∞ (resp. H_2) norms. This synthesis thus allows us to minimize different H_2/H_∞ norms
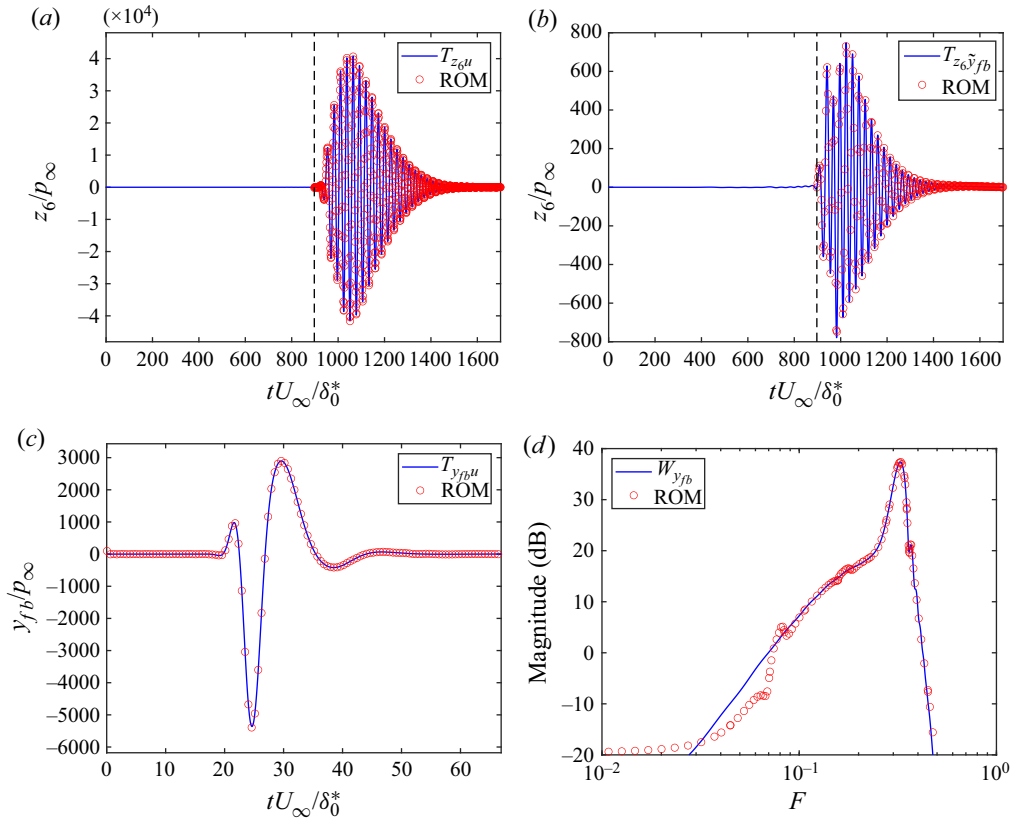
Figure 6. (*a*–*c*) Comparison between impulse responses (blue lines) and the ROMs (red circles) for the performance sensor z_6 and for the feedback estimation sensor y_{fb}. Note that for the ROMs of $T_{z_6 u}$ and $T_{z_6 \tilde{y}_{fb}}$, the time axes of the impulse responses are shifted by $\tau_{z_i \tilde{y}} U_\infty / \delta_0^* \approx 897$ (black dashed lines), which corresponds to the suppression of unnecessary dead times. (*d*) Comparison between the quantity $W_{y_{fb}}$ from the linear simulation (blue line) and the ROM (red circles).

under closed-loop stability constraints despite model uncertainties Δ. The structure of the controller K is defined by the user independently from the order of the state-space model to be controlled, which makes it a particularly powerful and flexible synthesis method. The set of transfer functions subject to an H_2/H_∞ norm minimization or constraints constitutes the augmented plant; these transfer functions are composed of the transfers of the controlled system allowing us to respect the specifications, along with weighting functions (Skogestad & Postlethwaite 2005). Weighting functions act as frequency domain constraints in order to shape adequately the transfer functions to achieve specific design goals. Furthermore, weighting functions allow us to normalize the different requirements to be able to balance them during the constrained minimization problem.

In our specific study, the structure of the controller K is imposed beforehand in the following way: (1) the controller K is searched in a state-space representation form; (2) the controller K must be stable; (3) we limit the controller order to 5 as high-order controllers are less easily implemented in practice (Goddard & Glover 1995); (4) we impose a tridiagonal state matrix that has significantly fewer parameters to determine than the full matrix, given that any real square matrix is similar to a real tridiagonal form
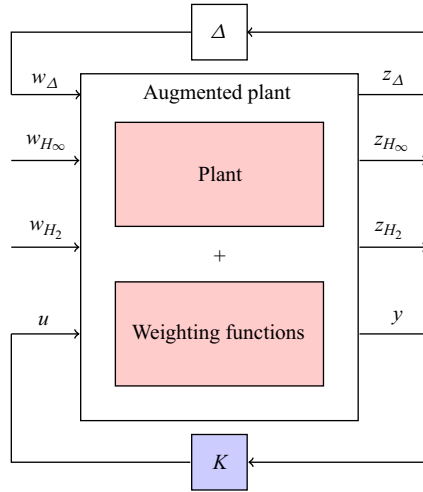
Figure 7. Multiple requirements H_2/H_∞ synthesis.

(McKelvey & Helmersson 1996); (5) we impose a strictly proper controller involving a natural roll-off of the high frequencies -20dB per decade in order to neglect dynamics in high frequencies and to be robust to high-frequency noise on the estimation sensor y naturally present in every experimental set-up. For the controller structure imposed above, the algorithm then solves the following constrained minimization problem:

$$\text{minimize} \quad \max_{i=1,\ldots,6} (\|T^c_{z_i w}\|_2),$$
$$\text{subject to} \quad \|W_S S\|_\infty < 1 \text{ and } \|W_{KS} KS\|_\infty < 1. \tag{5.3}$$

This constrained minimization problem is the transcription of the fluidic specifications established throughout § 4.

First, the minimization of H_2 norms of $T^c_{z_i w}$ directly allows the reduction of the expected power for the six performance sensors z_i used in the synthesis when they are excited by white-noise perturbations w and sensed by the estimation sensor y. A multi-objective synthesis approach is necessary for our problem by minimizing the expected power of sensors at different abscissa of the flat plate instead of minimizing an overall energy. Indeed, the disturbance energy growing as it is convected downstream, an overall energy would then essentially account for the fluctuating energy downstream of the domain, leaving aside the structures further upstream in the case of a very large computational domain. Transition to turbulence appearing locally above a certain perturbation energy threshold (see § 4.1), we advocate the need for minimizing the largest H_2 norm of the controlled system over the set of performance sensors z_i used to assess the local character of transition to turbulence.

Second, the H_∞ constraint on $W_S S$ maintains adequate stability margins. To prevent the closed loop from being unstable in a feedback design, a frequent choice is to ensure that $\|S\|_\infty < 2$ (Skogestad & Postlethwaite 2005; Belson *et al.* 2013). Thus the weighting function W_S has a constant frequency template such as $W_S(s) = 0.5$ because the H_∞ constraint on $W_S S$ is equivalent to $|S| < 1/|W_S| \ \forall \omega \in \mathbb{R}$. This means that the system will be guaranteed stable up to 50 % of relative model errors Δ on T_{yu} (see § 4.2). In the case of a feedforward design, $S(s) = 1$ (because $T_{yu} = 0$), and this H_∞ constraint is always satisfied, which explains the unconditional stability of the feedforward configuration.

Finally, the H_∞ constraint on $W_{KS}KS$ is here to desensitize the controller to new noise sources on a certain bandwidth. Our controller being already robust to high-frequency uncertainties due to the strictly proper structure imposed, W_{KS} is just designed to limit low-frequency actuator activity in case, for example, of low-frequency noise on the estimation sensor y.

By minimizing the maximum value between several transfer functions and using H_∞ norm constraints, a non-smooth optimization is performed; as non-smooth optimization is computationally intensive (compared to LQG synthesis), it is all the more important to obtain ROMs with the least possible states (see § 5.1), giving in our case computations of several tens of minutes.

6. Feedforward versus feedback control

6.1. *Performance on the nominal case*

The results of both feedforward (denoted 'Ff') and feedback (denoted 'Fb') controllers resulting from the constraint minimization problem (5.3) are evaluated by implementing the controllers in the DNS solver elsA. The implementation consists in solving the first-order differential equations of the controller state-space representation at different time steps of the simulations to update the control signal $u(t)$ from the estimation measurement $y(t)$:

$$\left. \begin{aligned} \dot{x}(t) &= A\,x(t) + B\,y(t), \\ u(t) &= C\,x(t), \end{aligned} \right\} \tag{6.1}$$

where $x \in \mathbb{R}^{5 \times 1}$ is the state vector, $A \in \mathbb{R}^{5 \times 5}$ is the state matrix, $B \in \mathbb{R}^{5 \times 1}$ is the input matrix, and $C \in \mathbb{R}^{1 \times 5}$ is the output matrix. The state vector equation is solved with a backward differentiation method of the second order. Figure 8(*a*) shows the sensitivity function S for the feedback design that respects the H_∞ constraint on the sensitivity function (i.e. $|S| < 1/|W_S| = 6$ dB) imposed in the minimization problem (5.3) (represented by the black dashed line). As explained previously, for the feedforward design, $|S| = 1$ (red line) and the constraint is satisfied automatically. Figure 8(*b*) represents $|KS|$ for both the feedforward and feedback cases. The weighting function W_{KS}, which allows us to limit actuator activity in case of low-frequency disturbances, is also shown, and we verify that $|KS| < 1/|W_{KS}| \; \forall \omega \in \mathbb{R}$. For the feedback design, $|KS|$ is close to $1/|W_{KS}|$ at low frequencies, meaning that there is a trade-off between minimizing H_2 norms and desensitizing the controller in the low-frequency range. We notice the natural roll-off of the controllers of -20 dB per decade at high frequencies related to the strictly proper structure imposed in the synthesis.

The control results in a significant reduction in the local H_2 norm of the transfers $T_{z(x)w}$ at each abscissa of the plate (see figure 8*c*) for both the feedforward and feedback configurations. As expected from the literature (Belson *et al.* 2013; Juillet *et al.* 2013; Semeraro *et al.* 2013*b*; Tol *et al.* 2019), the feedforward design minimizes the local H_2 norm even more than the feedback one. Nevertheless, for both configurations, the minimization of the cost functional $\max_{i=1,\dots,6}(\|T^c_{z_iw}\|_2)$ allowed the local H_2 norm of $T_{z(x)w}$ not to exceed, before $x = x_6$, a threshold given by the H_2 norm at $x = x_1$. Thus both configurations successfully achieve the control strategy set forth in figure 2. The use of an H_2 performance criterion alongside the H_∞ criterion on the stability margin allows to address both performance in terms of disturbance rejection and stability robustness in the design of the feedback loop.
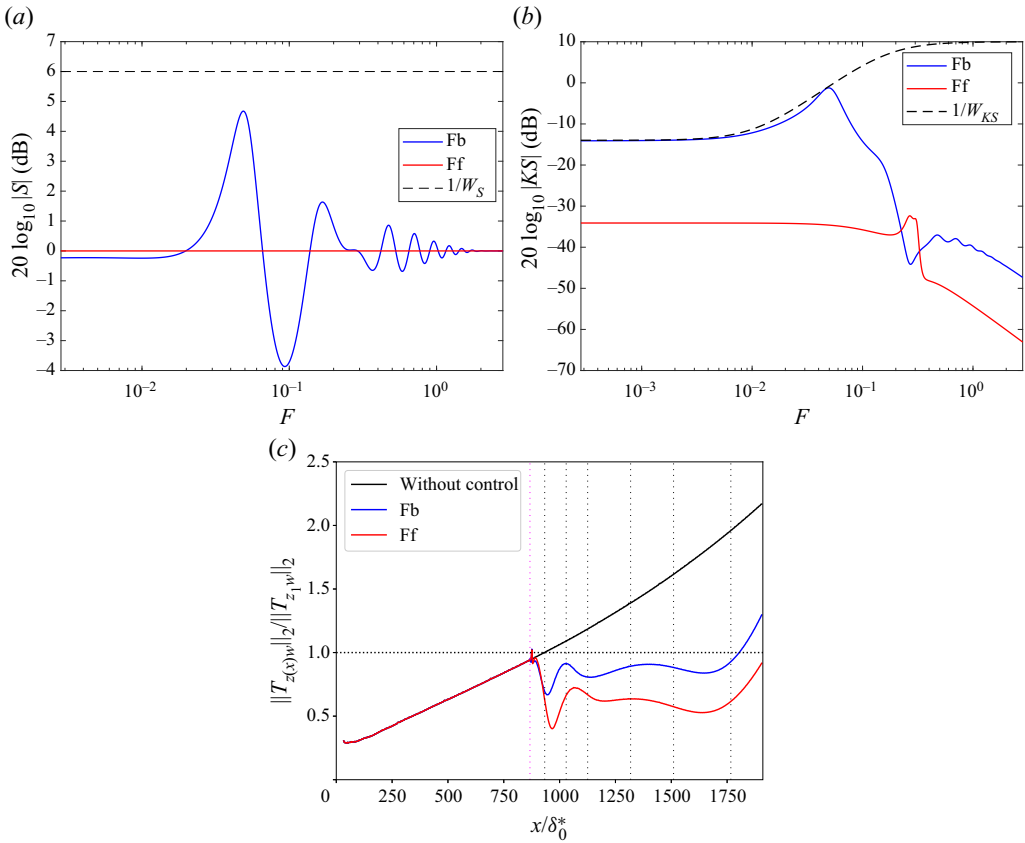
Figure 8. Blue, red and dashed lines represent the feedback case, the feedforward case and the constraints (weighting functions) imposed for the control design, respectively. (*a*) Magnitude of S. (*b*) Magnitude of KS. (*c*) Evolution of the local H_2 norm of the transfer $T_{z(x)w}$ as obtained from the DNS simulation. (Those obtained with the ROMs are actually identical at $x = x_i$ since the ROMs are very accurate.) The vertical magenta and black dotted lines represent, respectively, the position of the actuator (with the sensors y_{fb} and y_{ff} nearby) and the six performance sensors z_i used for synthesis. The values are normalized by $\|T_{z_1w}\|_2$. The horizontal black dotted line depicts the energy threshold $\|T_{z_1w}\|_2$ respected until x_6 following the minimization of the cost functional $\max_{i=1,\dots,6}(\|T_{z_iw}^c\|_2)$.

In addition to the reduction of the local H_2 norm along the plate, the local H_∞ norm $\|T_{z(x)w}\|_\infty$ has also decreased for both the feedforward and feedback designs (see figure 9); this variation is directly related to the N-factor envelope $\tilde{N}$ by

$$\max_{x_1<x<x_6} \ln \|T_{z(x)w}\|_\infty - \max_{x_1<x<x_6} \ln \|T_{z(x)w}^c\|_\infty = \max_{x_1<x<x_6} \tilde{N} - \max_{x_1<x<x_6} \tilde{N}^c. \qquad (6.2)$$

More precisely, feedforward and feedback designs respectively 'save' 1.13 and 0.89 points of N-factor. One might ask which is the most effective set-up for delaying transition, between minimizing $\max_i(\|T_{z_iw}^c\|_2)$ and minimizing $\max_i(\|T_{z_iw}^c\|_\infty)$, but answering this question is beyond the scope of this study.

In addition to these results on wall-pressure fluctuation sensors coming from impulse responses, we consider the global root-mean-square (r.m.s.) temperature field (denoted T'_{rms}) and streamwise velocity field (denoted u'_{rms}). For T'_{rms}, whose high values are located
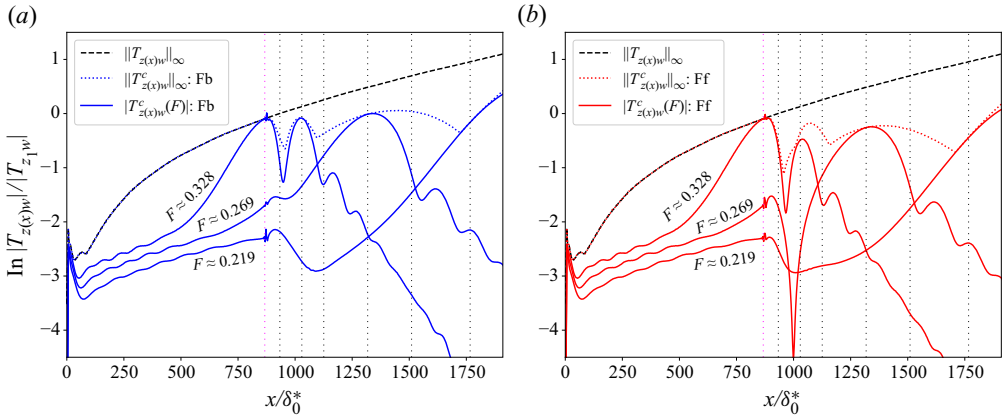
Figure 9. Evolution of the local H_∞ norm of the transfer $T_{z(x)w}$ as a function of the plate abscissa for the uncontrolled (black dashed lines) and (*a*) feedback and (*b*) feedforward cases. The evolution of $|T^c_{z(x)w}(F)|$ for some frequencies is also shown for the controlled cases. Vertical lines are as in figure 8(*c*).

around the generalized inflection point (white dashed line) in the uncontrolled case (see figure 10*a*), the control reduces the amplitude of the perturbations (see figure 10(*b*) for the feedback case). For the field u'_{rms} in the uncontrolled case (see figure 10*c*), high-level regions are localized close to the wall. These levels are decreased drastically when control is present (see figure 10(*d*) for the feedback case). Regarding the feedforward design (not shown here), it further reduces the amplitude of disturbances (as in figure 8*c*). By drastically reducing the amplitude of velocity disturbances in both feedforward and feedback configurations, while the controllers were built from wall pressure fluctuation performance sensors, one may hope to strongly delay transition to turbulence due to the second Mack mode in a 3-D set-up. The question of the energy efficiency of the control is left to Appendix D as the gain cannot be computed in terms of saved drag; the gain is calculated in this study in terms of mean Chu energy flux reduction, which is not the quantity that one seeks to reduce in realistic 3-D configurations. Stability and performance robustness are addressed further next.

6.2. *Stability robustness*

In the case of the feedback design, the configuration can be unstable and it is necessary to quantify the evolution of the stability margins following inflow condition variations or uncertainties. The closed-loop system is stable if and only if the Nyquist plot of the loop gain $-T^{real}_{yu}K$ (which is stable) does not encircle the critical point $(-1, 0)$. As discussed already in § 4.2, the Nyquist plot of $-T_{yu}K$ therefore allows us to quantify the available stability margins related to the distance to the critical point by visualizing the maximum amount of error $|\Delta|$ admissible before instability sets in. The gain and phase margins (denoted *GM* and *PM*) respectively represent the minimum amount of gain and phase variations required to lose stability. In our case, the gain and phase margins respectively stand for an estimation error in the instability's growth rate and convection speed that can lead to an instability of the feedback loop (Sipp & Schmid 2016). Inlet velocity variation is considered here to be the most problematic variation (compared to other primitive variable variations) as it involves multiple changes: (i) variation in time delays due to change in convection velocity; (ii) modification of the Reynolds number Re_x, implying that for a
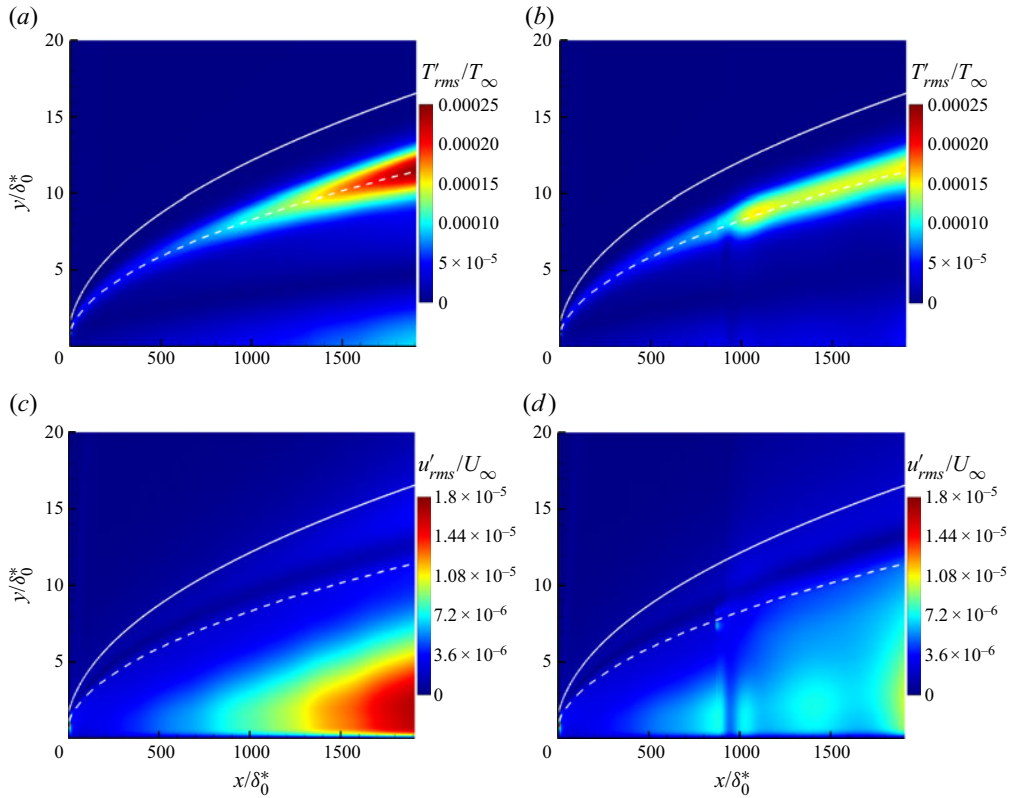
954 A20-24

Figure 10. Contours of (a,b) T'_{rms} and (c,d) u'_{rms}, for the (a,c) uncontrolled and (b,d) feedback cases. The white solid lines and dashed lines represent the boundary layer thickness δ and the generalized inflection point position y_g, respectively.

given abscissa on the domain, the dominant frequencies are higher (resp. lower) after an increase (resp. decrease) of Re_x; (iii) variation of the Mach number M_∞, implying a modification of the neutral curves and by extension a modification of the growth rates. For a variation of the upstream velocity at the entry of the domain U_∞ of $\pm 5\,\%$, which induces $M_\infty \in [4.275, 4.725]$, the new transfer functions $T_{yu_{\pm 5\,\%}}$ are compared with the reference one T_{yu} in figures 11(a) and 11(b). The greatest variations for the module appear to be around $F = 0.423$; we notice that a 5 % increase of the upstream velocity implies a greater maximum value for the module at a slightly lower frequency, whereas a 5 % decrease in velocity implies a smaller maximum value for the module at a slightly higher frequency (see figure 11a). The variation of $\pm 5\,\%$ of the inlet velocity leads to the modification of the delays, represented by the slope of the phase versus frequency plot (see figure 11b): for the 5 % increase of the upstream velocity, the absolute value of the slope is less and the delay is therefore shorter (with a relative variation for the delay of 3.4 % compared to the reference case), whereas the opposite is obtained in the case $-5\,\%$ (with relative variation 3.9 % for the delay). Figures 11(c) and 11(d) show the Nyquist plots of the loop gains $-T_{yu}K_{fb}$ and $-T_{yu_{\pm 5\,\%}}K_{fb}$. The variations of the upstream velocity slightly alter the stability margins compared to those obtained in the reference case: the phase margin stays infinite, while the gain margin GM (black dashed lines) and the modulus margin $\|S\|_\infty^{-1}$ (black dotted lines) fluctuate respectively by a maximum of 3.6 % and 5.1 %, while remaining far from
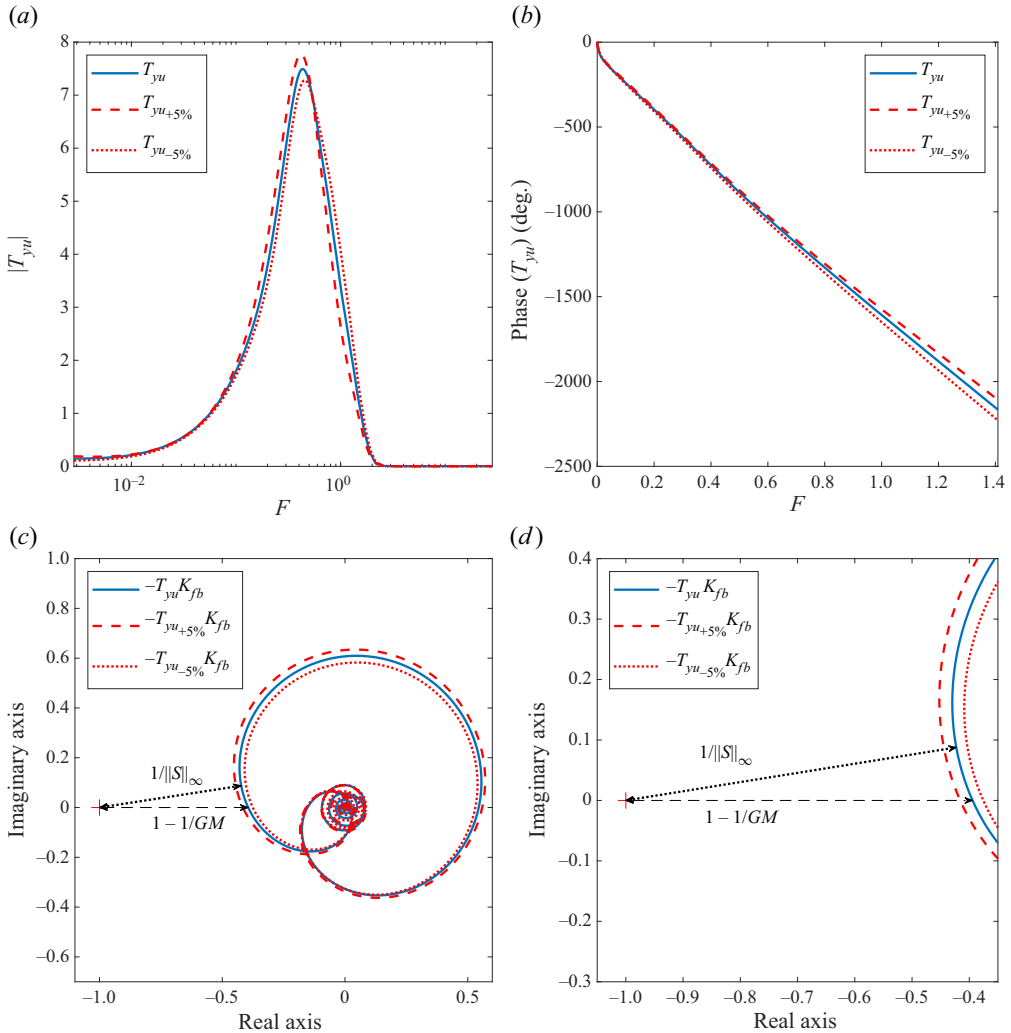
954 A20-25

Figure 11. Evolution of the module (*a*) and phase (*b*) of T_{yu} after a variation of $\pm 5\,\%$ of the inlet velocity. Global view (*c*) and zoom near the critical point $(-1, 0)$ (*d*) of the Nyquist plot of the loop gain $-T_{yu}K_{fb}$ (solid blue line) and $-T_{yu\pm 5\,\%}K_{fb}$ (dashed and dotted red lines). The black dotted line represents the modulus margin $\|S\|_\infty^{-1}$ (the minimal distance to instability). The black dashed line represents the gain difference before instability and is linked to the gain margin *GM*.

the critical point. Given the small impact of the inflow velocity variations of $\pm 5\,\%$ on all margins, the feedback design may be stable for even greater velocity variation. Therefore, unlike previous feedback studies using LQG synthesis (Barbagallo *et al.* 2012; Tol *et al.* 2019), the robustness to stability for a feedback design obtained with a robust synthesis method is not a problem. Next, we examine performance robustness, which is a different issue.

6.3. *Performance robustness*

Robustness to performance is evaluated by checking that the control laws remain efficient in terms of expected power reduction of the different performance sensors z_i
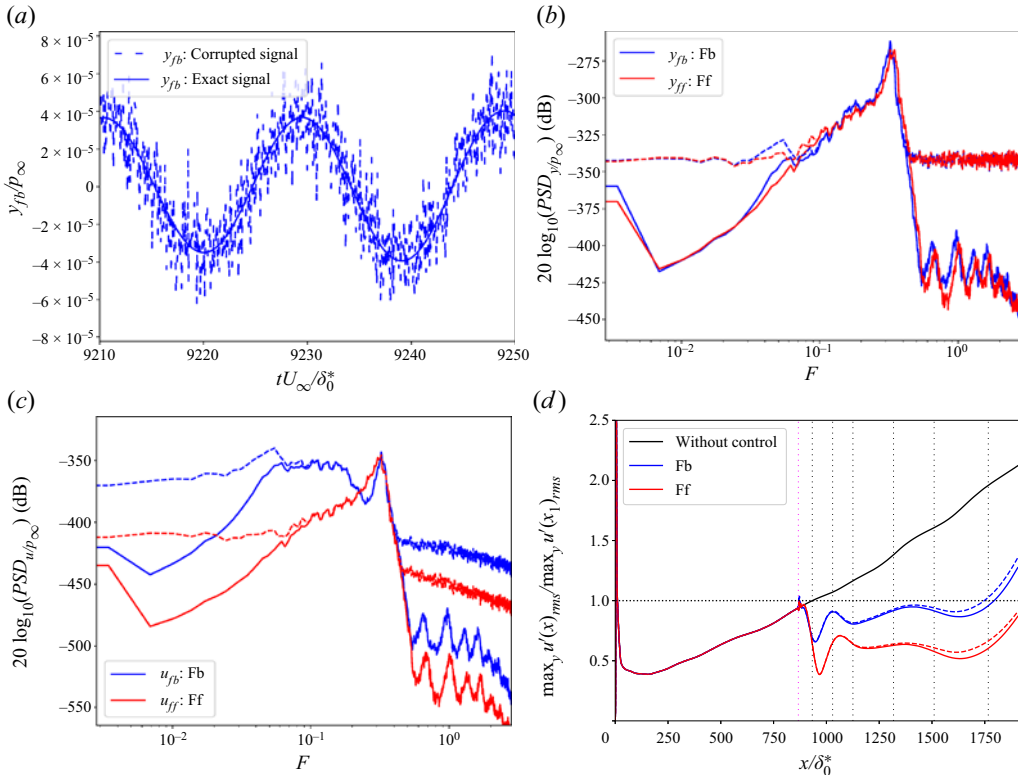
Figure 12. In all plots, feedback and feedforward designs are represented by blue and red lines, respectively. Controlled systems with ideal and noisy estimation sensors are represented by solid and dashed lines, respectively. (*a*) Short sequence of y_{fb} corrupted by 50 % of the r.m.s. value without control of y_{fb}. Comparison of the evolution of PSD_y (*b*), PSD_u (*c*) and $\max_y u'_{rms}$ (*d*) for the controlled systems with ideal and noisy estimation sensors. The details for (*d*) are the same as in figure 8(*c*).

despite new noise sources or differences between on-design and off-design operating conditions.

6.3.1. *Noisy sensors*

Noisy estimation sensors are modelled by adding white Gaussian noise on both y_{fb} and y_{ff} (see figure 12a). Both estimation sensors are corrupted by the same amount of noise (50 % of the r.m.s. value without control of y_{fb}), which models an intrinsic defect of the sensor, such as electronic noise, that does not depend on its position along the domain. Nevertheless, the streamwise position of y_{ff} being quite close to that of y_{fb}, the ideal signal-to-noise ratio remains very similar for both configurations and varies by only a few per cent. The PSD of the corrupted estimation sensors remains unchanged in the frequency band of the second Mack mode but exhibits much larger values in low and high frequencies (see figure 12b). This is because the PSD of white noise being constant, the ideal signal-to-noise ratio is particularly low for frequencies where the ideal signal energy is low. The signal y is given to the controller K, which generates the actuator signal u; the control signal PSD for corrupted signals y becomes stronger on the previously mentioned low- and high-frequency bands, compared to the PSD of u for ideal signals y

(see figure 12c). Nevertheless, thanks to the strictly proper structure and the filter W_{KS} imposed in the synthesis step, $|KS|$ has been constrained in these frequency bands. Thus the actuator activity remains limited in these regions despite the important added noise, and if we look at the evolution of the maximum along the wall-normal direction of u'_{rms} (denoted $\max_y u'_{rms}$), then we keep a performance close to the ideal case (see figure 12d). Both feedback and feedforward configurations stay below the velocity energy threshold until x_6, and these two designs are robust to noise on the estimation sensors. If even noisier sensors were used, then it would suffice to decrease the amplitude of the weighting function $1/W_{KS}$ to recover performance robustness (especially in low frequencies for the feedback configuration). For the case illustrated in figure 12, a higher $1/W_{KS}$ (involving a less constrained controller) could lead to an excessive injection of energy in the vicinity of the actuator (see Appendix E).

6.3.2. *Off-design operating conditions*

Performance robustness to off-design operating conditions is assessed by considering the evolution of the local H_2 norm of $T_{z(x)w}$ after a variation of free-stream density ρ_∞ and velocity U_∞ of $\pm 5\,\%$, for both feedback and feedforward cases. The density variation may correspond in practice to a change in altitude, whereas the velocity variation may correspond to a change in cruise speed. When ρ_∞ is modified, the temperature and velocity inlet values are kept constant, which means that M_∞ and hydrodynamic delays related to the convective behaviour are maintained (see the green dashed line figure 13a) while only Re_x is modified (which implies a change in the dominant frequencies at a given abscissa, as seen in figure 13b). A modification of U_∞, on the other hand, has a much more dramatic effect since it implies variations of time delays (see the purple dashed line figure 13a), which will ultimately impact the only important residual delay, which is the one between the actuator and the estimation sensors. It will also impact the values of Re_x and M_∞, which modify the base-flow profiles. Changing the base flow impacts the stability characteristics of the boundary layer, and, in turn, the dominant frequencies along the plate, as seen in figure 13(b).

With density variations of $\pm 5\,\%$ (see figure 13c), despite degraded off-design performance, both feedback and feedforward controllers manage to reduce the local H_2 norm compared to the case without control over a fairly large distance on the flat plate. However, while the feedforward design minimized the local H_2 norm more than the feedback one for the nominal case (solid lines), it seems that this is no longer necessarily the case in off-design situations (dotted and dashed lines). The variation in performance between the nominal and off-design cases in the feedback configuration appears less pronounced than in the feedforward set-up, which is allowed by the sensitivity function S. Although this transfer function, because of the delay due to the actuator/estimation sensor distance, limits the achievable performance on the nominal case for a feedback setup (see Appendix B), it allows us to desensitize the system to modelling errors or to variations in system characteristics over a certain bandwidth. Even if both designs exceed the H_2 norm threshold at some point, they have some robustness to performance with respect to density variations by staying below the uncontrolled system H_2 norm all along the domain.

The real strength and superiority of the feedback design over the feedforward one lies in its ability to maintain correct performance during velocity variations (see figure 13d). While the feedback set-up manages to maintain some performance in off-design conditions by staying below the local H_2 norm of the uncontrolled system over a fairly long distance along the plate, the feedforward design fails to maintain the performance requirement by
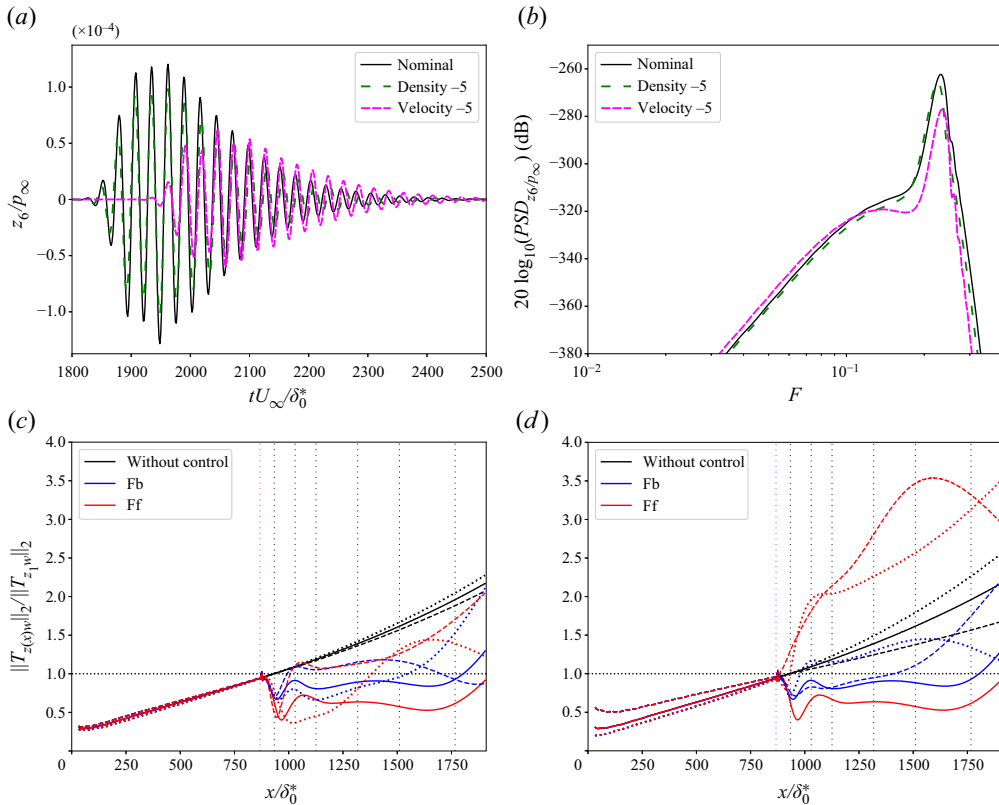
Figure 13. Comparison of uncontrolled pressure wavepackets generated by an impulse of w (a) and their PSD (b) at x_6 after a variation in ρ_∞ and U_∞ of -5%. Evolution of the local H_2 norm of $T_{z(x)w}$ after a variation in ρ_∞ (c) and U_∞ (d) of $\pm 5\%$ (dotted and dashed lines). The nominal cases are in solid lines. See caption of figure 8(c).

amplifying the local H_2 norm. This increase in the feedforward set-up may then lead to a faster transition to turbulence, which is the opposite of the desired objective. The velocity variations, regardless of changes in Reynolds and Mach numbers, are indeed particularly problematic as they modify the residual delay τ_{yu}, which directly impacts (5.1) and (5.2), and therefore may cause the controllers to activate out of phase. Thus in the case of noise-amplifier flows, we underline the importance of assessing the robustness to performance with respect to velocity variations, as in Fabbiane *et al.* (2015). One could be tempted to robustify the feedforward set-up by using an adaptive controller structure (Fabbiane *et al.* 2014), but this type of approach is robust only at long times (subject to convergence of the method), and the problem of robustness following abrupt velocity variations would remain. Therefore, as soon as variations or uncertainties on the inflow velocity are present, the best trade-off between performance and robustness is a feedback configuration.

7. Conclusions

A robust reactive control method has been developed in order to control the linear growth of the second Mack mode in a 2-D boundary layer over a flat plate at Mach 4.5. The control

tools (for identification and synthesis) being mathematically well-established in a linear framework, they are perfectly suited for this precise scenario of transition to turbulence where we seek to control the linear growth of small perturbations.

The choices of the types and positions of the actuator and sensors are based on the study of the noise-amplifier behaviour of our flow, in order to trigger the optimal growth mechanisms and ensure efficient flow control. During the identification step, some unnecessary dead times related to the convective nature of the flow are removed, allowing a significant reduction in the size of the ROMs, which is beneficial for both the identification and synthesis steps. Moreover, we strive to identify only quantities that could be obtained in an experimental set-up.

After identifying these useful transfers through data-driven methods, the synthesis of the controllers is achieved with a structured mixed H_2/H_∞ synthesis. This robust synthesis method allows us to limit the order of the controller, to impose its structure up front, and to constrain simultaneously several transfer functions to obtain at the same time performance and robustness. Instead of simply minimizing a global energy, the constraint minimization problem is posed in such a way that a shaping of the spatial evolution of different local energy measures is realized, which seems a more suitable approach to delay transition to turbulence. Multiple performance sensors in the streamwise direction are therefore needed in this study to cover the entire spectrum of amplified frequencies along the domain, and to capture the non-modal transient growth effect generated by the actuator.

After implementing the control laws in the elsA solver, we find that feedforward and feedback designs both manage not to exceed a certain energy threshold in the nominal case. Moreover, the stability robustness for the feedback design is not a problem thanks to the robust synthesis and the constraints imposed. Regarding performance robustness, both feedforward and feedback designs manage to reduce the amplitude of disturbances compared to the uncontrolled case, despite noisy estimation sensors or inflow density variations. Nevertheless, for noise-amplifier flows, we stress the importance of assessing robustness to performance by changing the inflow velocity. Indeed, this type of variation may cause the controller to activate out of phase. It appears that the feedforward set-up is completely unable to follow inflow condition variations, while the feedback set-up keeps reasonable performance over a large velocity variation of $\pm 5\,\%$. Therefore, the best trade-off between performance and robustness requires a feedback configuration (in the case of a linear time-invariant controller). This result looks contradictory to conventional wisdom, which favours a feedforward set-up for noise-amplifier flows. The widespread use of a feedforward structure is likely rooted in the massive use of LQG synthesis for the control of noise-amplifiers. Indeed, LQG synthesis comes with no guaranteed stability margin, which hinders its practical application to a feedback set-up. Belson *et al.* (2013) were among the first to recognize the superiority of a feedback design for performance robustness in noise-amplifier flows. The authors used loop-shaping on a simple PI controller, but much richer feedback laws may be designed in a systematic way using the modern robust synthesis tools of the present paper. Such tools are already commonly used for the control of oscillator flows, where feedback is mandatory to stabilize the unstable base flow (Flinois & Morgans 2016; Leclercq *et al.* 2019; Shaqarin *et al.* 2021). We expect the methodology of the present paper, based on data-driven identification and robust synthesis on a feedback set-up, to be relevant to other convectively unstable flows.

We are currently extending this study to a 3-D case with the goal of delaying transition to turbulence. This implies placing multiple estimation/performance sensors and actuators

in the transverse direction, and controlling oblique waves of the first Mack mode as well as nonlinearities.

Author ORCIDs.

Pierre Nibourel https://orcid.org/0000-0002-3229-8580;

Colin Leclercq https://orcid.org/0000-0002-8262-0697;

Fabrice Demourant https://orcid.org/0000-0002-3354-9353;

Eric Garnier https://orcid.org/0000-0001-8944-3809;

Denis Sipp https://orcid.org/0000-0002-2808-3886.

Appendix A. Base-flow and growth rates validation

The ability of the spatial schemes to compute accurately base and perturbed flows is evaluated by comparing with the results of Ma & Zhong (2003). This 2-D test case consists of a uniform flow at $M_\infty = 4.5$ on an adiabatic flat plate. The numerical domain extends over $0 < Re_x \lesssim 4.1 \times 10^6$ in the streamwise direction, and the wall-normal extent of the domain is taken to be $\sim 24\,\%$ of the streamwise length. The free-stream conditions and the mesh grid are similar to those in § 3. The boundary conditions also correspond to those used previously, except that a uniform state in the wall-normal direction is prescribed at the supersonic inlet, and the sponge area is removed to correspond to the Ma & Zhong (2003) configuration. Good agreement is achieved for both wall-pressure distribution (see figure 14a) and second wall-normal streamwise derivative velocity profile $\partial_y^2 u$ at $Re_x = 1 \times 10^6$ (see figure 14b). In addition, the ability of spatial schemes to capture correctly the perturbations q' is evaluated. It is assessed by comparing the spatial growth rate $-\tilde{\alpha}_i = (1/|\tilde{p}(x, y = 0)|)\, \partial_x |\tilde{p}(x, y = 0)|$ evaluated from the response field of the resolvent analysis (solid line) and from Fourier transform results of Ma & Zhong (2003) on linearized DNS (blue circles; see figure 14c) for the frequency $F = 0.34$. This frequency is close to the dominant frequency at the actuator streamwise position in our study (see figure 5b). For their linearized DNS, Ma & Zhong (2003) force waves from the inlet boundary condition by specifying the flow as the superposition of the steady base flow and a temporal fluctuation of flow variables. Hence, to compare their results to the global stability approach, the forcing field $\tilde{f}$ for the resolvent optimization problem is constrained to a thin strip $\sqrt{Re_x} \in [476.67, 483.3]$ localized far upstream of the locally unstable region; outside this region, the forcing field is set to zero. This streamwise restriction is sufficiently far upstream to ensure that the component-type non-normality effects no longer dominate in the modal instability domain of $F = 0.34$ to compare with Ma & Zhong (2003). The domain involved in the streamwise direction for the Chu energy optimization of the response field is $\sqrt{Re_x} \in [476.67, 1998.1]$. In the wall-normal direction, no restriction is applied for the domains involved in the definition of $\|\cdot\|_E^2$ and $\|\cdot\|_F^2$. Good agreement is achieved between the evolution along x of the quantity $-\tilde{\alpha}_i$ from our resolvent analysis and the one from linearized DNS of Ma & Zhong (2003). The growth rate $-\alpha_i$ from our in-house LLST code is also plotted, and exhibits values similar to $-\tilde{\alpha}_i$ in the LLST instability region. As the configuration of Ma & Zhong (2003) is very similar to the one in our study, these results validate the spatial schemes used to describe the base flow and the 2-D perturbation field.
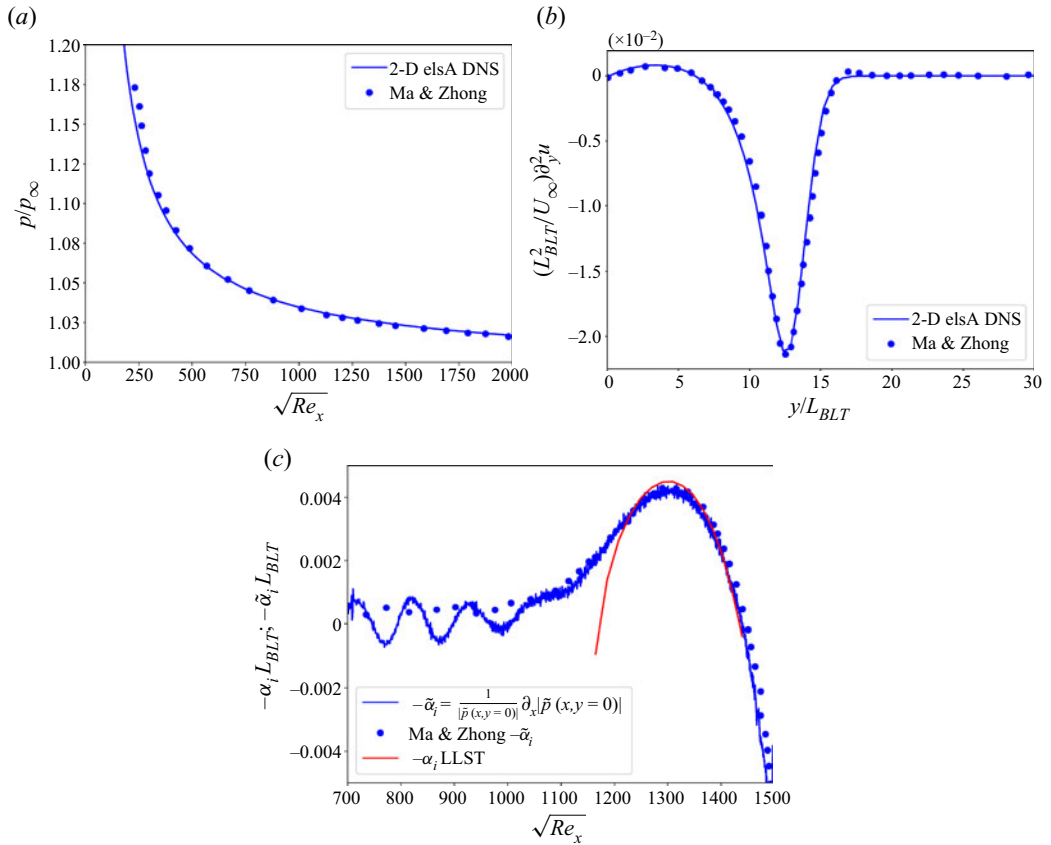
Figure 14. Comparison of (*a*) wall-pressure distribution and (*b*) second wall-normal streamwise derivative velocity profile at $Re_x = 1 \times 10^6$ with results from Ma & Zhong (2003). (*c*) Comparison of $-\tilde{\alpha}_i = (1/|\tilde{p}(x, y = 0)|)\, \partial_x|\tilde{p}(x, y = 0)|$ from our resolvent analysis (blue solid line) and from the Fourier transform of (Ma & Zhong 2003) on linearized DNS (blue circles) at $F = 0.34$. The growth rate $-\alpha_i$ (red line) computed with our in-house LLST code is also plotted. In (*b*) and (*c*), lengths are made dimensionless using the length scale of the boundary layer thickness $L_{BLT} = \sqrt{\mu_\infty x / \rho_\infty U_\infty}$.

Appendix B. Position of the estimation sensor

To obtain the quantitative position of the sensor y in our supersonic boundary layer study for both feedforward and feedback configurations, a quick analysis is carried out. It consists in looking at the impact of the actuator/measurement sensor distance on the maximum achievable performance in terms of H_2 norm reduction on the performance sensor z_6 regardless of the desensitization to low-frequency disturbances (see § 5.2). We consider only the performance sensor z_6 because it is the one furthest downstream of the domain; the further downstream we are, the more we have to reduce the local H_2 norm in order not to exceed a given threshold (see the explanatory diagram in figure 2*c*). This performance sensor therefore plays a central role, and the position of the estimation sensor y must allow a consequent reduction of the energy of the sensor z_6. Since this analysis is done only off-line on the ROMs, and the resulting controller is not implemented on the real complete system, the $\|W_{KS}KS\|_\infty$ constraint that was useful only in case of new noise sources (as noisy estimation sensor) is disabled.
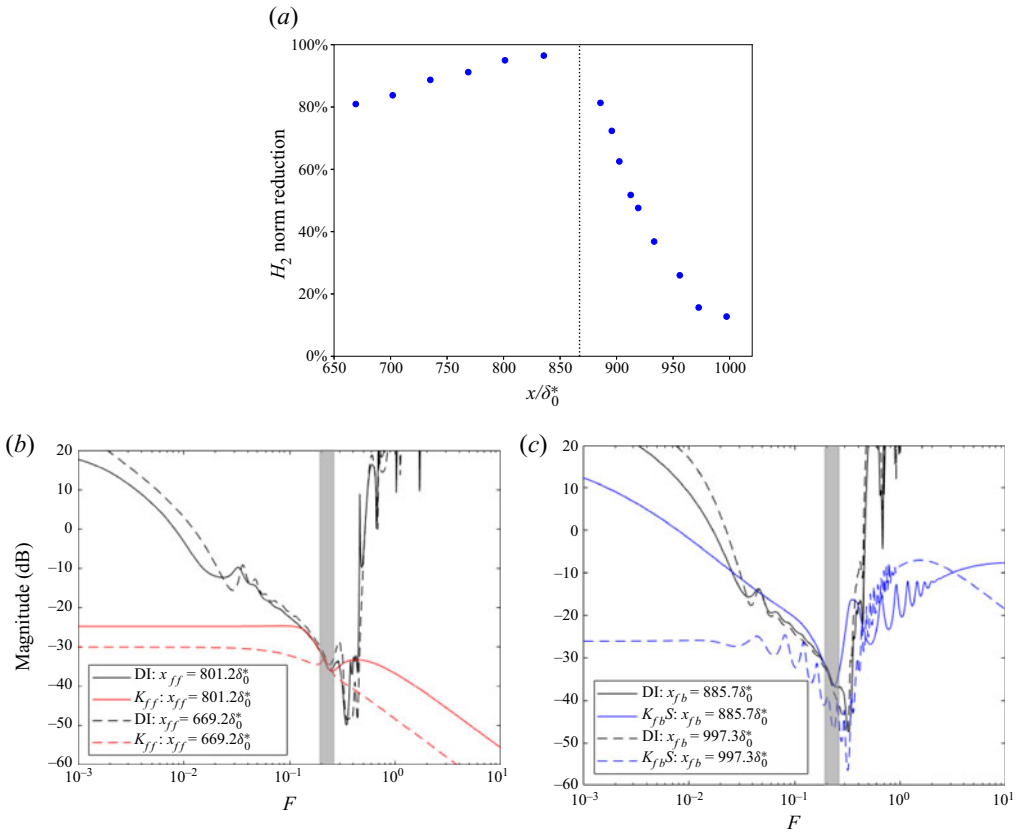
(*a*)

(*b*)

(*c*)

Figure 15. (*a*) Evolution of the maximum performance achievable of the ROM of the sensor z_6 as a function of the position of the measurement sensor *y*. The dotted line represents the actuator position; feedforward and feedback are respectively to the left and right of this dotted line. Comparison of the gains of the controllers from the structured synthesis and those from ideal destructive interference case (denoted 'DI') for (*b*) feedforward and (*c*) feedback configurations. The grey shaded area represents the range of the dominant frequencies of the sensor z_6.

For the controller structure developed in § 5.2, the constraint minimization problem (5.3) is therefore written as

$$\text{minimize} \quad \|T^c_{z_6 w}\|_2,$$
$$\text{subject to} \quad \|W_S S\|_\infty < 1. \tag{B1}$$

Figure 15(*a*) shows the evolution of the maximum performance achievable of the ROM of the performance sensor z_6 as a function of the actuator/measurement sensor distance. The H_2 norm reduction represents the quantity $(\|T^c_{z_6 w}\|_2 - \|T_{z_6 w}\|_2)/\|T_{z_6 w}\|_2$. On the one hand, the actuator/measurement sensor distance influences very strongly the maximum performance achievable for feedback designs (to the right of the dotted line). On the other hand, feedforward designs (to the left of the dotted line) are relatively unaffected by this distance over a certain range, and they perform better than feedback ones, which is consistent with the results of the incompressible literature (Belson *et al.* 2013; Juillet *et al.* 2013; Freire *et al.* 2020). Controllers from the structured synthesis are compared with those that would have created perfect destructive interferences (denoted 'DI') on the whole frequency spectrum at x_6 (see figures 15*b*,*c*); indeed, a perfect wave cancellation at

x_6 for each frequency is obtained for

$$z_6^c = 0 = (T_{z_6\tilde{y}} + T_{z_6u}KS)\tilde{y},$$
$$KS = -T_{z_6\tilde{y}}/T_{z_6u}. \quad\quad\quad\quad (B2)$$

To get rid of the problems of stability and causality that occur when T_{z_6u} is inverted directly, the ratio $-T_{z_6\tilde{y}}/T_{z_6u}$ is constructed frequency-by-frequency. Hence this ideal DI quantity just allows us to evaluate how close the controllers obtained by structured synthesis are to the perfect cancellation (without taking into account feasibility, stability and robustness principles). The gain of K from structured synthesis for a feedforward estimation sensor y placed at $x_{ff} = 801.2\delta_0^*$ (red solid line) overlaps the ideal DI one (black solid line) in the range of the dominant frequencies of the sensor z_6 (grey shaded area); for a feedforward estimation sensor y placed at $x_{ff} = 669.2\delta_0^*$ (red dashed line), the gain is also very similar in the area of interest to the ideal DI gain. For a feedback configuration, the closer an estimation sensor is to the actuator, the more similar the controller resulting from the structured synthesis is to the DI case in the range of the dominant frequencies of the sensor z_6, which allows for large reduction of the H_2 norm. For a feedback sensor placed at $x_{fb} = 997.3\delta_0^*$ (blue dashed line), the resulting controller does not allow us to create perfect destructive interference, which explains the low performance obtained for this position. The rapid drop in performance in the feedback cases is largely due to the delay in T_{yu} (Belson *et al.* 2013), which is the time it takes for the wave generated by the actuator to arrive at the estimation sensor. For a transfer function T_{yu} with a time delay τ_{yu}, it is not possible to cancel out disturbances in a time scale shorter than τ_{yu} as a control at a time t has no effect until $t + \tau_{yu}$ (Glad & Ljung 2000); the controllable bandwidth f_c is limited by $f_c \lesssim 1/\tau_{yu}$ (Glad & Ljung 2000; Skogestad & Postlethwaite 2005). In other words, the actuator/measurement sensor distance $U_\infty\tau_{yu}$ must be less than $\sim U_\infty/f_c$. As a result, the frequency spectrum of the performance sensor z_6 containing a significant amount of energy up to $F \approx 0.282$, this requires an actuator/sensor distance of less than $2\pi\delta_0^*/F \sim 20\delta_0^*$ in this case. Then, to obtain significant performance in terms of amplitude reduction, it is decided to place the sensor y_{fb} for the feedback configuration at a distance $18.5\delta_0^*$ from the streamwise position of the actuator ($x_{fb} = 885.7\delta_0^*$). For the feedforward design, the sensor y_{ff} is placed at distance $66\delta_0^*$ from the streamwise position of the actuator ($x_{ff} = 801.2\delta_0^*$) in such a way as to ensure that it is possible to disregard T_{yu} in the synthesis while having an optimal performance.

Appendix C. Evolution of performance as a function of the number of sensors z_i used in the synthesis

For the two sensor positions x_{fb} and x_{ff} determined previously, the following minimization problem is solved:

$$\text{minimize} \quad \max_{z_i \in z_{used}} (\|T_{z_iw}^c\|_2),$$
$$\text{subject to} \quad \|W_S S\|_\infty < 1 \text{ and } \|W_{KS}KS\|_\infty < 1, \quad\quad (C1)$$

with the controller structure developed in § 5.2. Not all of the six performance sensors are necessarily used for the minimization problem, and the evolution of performance as a function of the number of sensors z_i (and by extension their positions) employed in the synthesis is assessed. The set of sensors z_i used in the synthesis is denoted z_{used}. In table 2, the different configurations tested are listed: the cases labelled 'Fbkz' (resp. 'Ffkz') stand for feedback designs (resp. feedforward designs) with k performance sensors used

Case	Sensors z used for synthesis	$\max\limits_{z_i \in z_{used}} \left(\dfrac{\|T^c_{z_i w}\|_2}{\|T_{z_1 w}\|_2} \right)$	$\max\limits_{x_1 < x < x_6} \left(\dfrac{\|T^c_{z(x)w}\|_2}{\|T_{z_1 w}\|_2} \right)$
Without control	—	1.96	1.96
Fb1z	$z_{used} = \{z_6\}$	0.41	9.03
Fb3z	$z_{used} = \{z_1, z_4, z_6\}$	0.67	1.98
Fb4z	$z_{used} = \{z_1, z_2, z_3, z_6\}$	0.90	1.06
Fb6z	$z_{used} = \{z_1, z_2, z_3, z_4, z_5, z_6\}$	0.92	0.92
Ff1z	$z_{used} = \{z_6\}$	0.14	2.48
Ff6z	$z_{used} = \{z_1, z_2, z_3, z_4, z_5, z_6\}$	0.67	0.73

Table 2. Evolution of the performance after the controllers are implemented in elsA as a function of the number of sensors z_i used in the synthesis step. Cases labelled 'Fbkz' (resp. 'Ffkz') stand for feedback designs (resp. feedforward designs) with k performance sensors used in the synthesis. The results are normalized by the local H_2 norm of the uncontrolled system at the position x_1.

in the synthesis; the performance sensors used for each case are also given. Assuming that the transition to turbulence process begins shortly after the streamwise position of the actuator, it is chosen to scale the results by the local H_2 norm of the uncontrolled system at the performance sensor z_1, which is the closest performance sensor to the actuator. The maximum local H_2 norm between the position of the sensors z_1 and z_6 (respectively, the most upstream and the most downstream performance sensors used in some syntheses) for the controlled system is denoted $\max_{x_1 < x < x_6} \|T^c_{z(x)w}\|_2$.

The resulting controllers are then implemented in elsA, and we focus on the evolution of the local H_2 norm of the transfers $T_{z(x)w}$ at each abscissa of the plate. The evolution of the local H_2 norm of the transfers $T_{z(x)w}$ for the case without control and the different feedback cases is depicted in figure 16(a) (for feedforward cases, these results are summarized in table 2). For the Fb1z and Ff1z cases, where the controller is designed to minimize the energy of the performance sensor z_6, this results in a strong reduction of the local H_2 norm at the end of the domain; in the feedback (resp. feedforward) configuration, $\|T^c_{z_6 w}\|_2$ is even about 4.78 (resp. 14.) times lower than $\|T_{z_6 w}\|_2$. However, this significant decrease in energy downstream of the domain was accompanied by a strong increase in the local H_2 norm upstream in the domain (blue dashed line in figure 16(a) for the feedback case). The quantity $\max_{x_1 < x < x_6} \|T^c_{z(x)w}\|_2$ for both feedforward and feedback configurations appears greater than the uncontrolled case; this increase of the local H_2 norm may then lead to a faster transition to turbulence in a 3-D set-up, which is the opposite of the desired objective.

This increase of the local H_2 norm can be explained from figure 16(b), which represents the module of $T_{z_6 w}$ (dashed lines) and $T_{z_1 w}$ (dotted lines) for the uncontrolled (black lines), Fb1z (blue lines) and Ff1z (red lines) cases. On the one hand, the amplitudes of the dominant frequencies of the uncontrolled system for the sensor z_6 (which is the only one used in the synthesis for these cases) are significantly reduced in both feedback and feedforward cases, which partly explains the significant reduction in the H_2 norm for this transfer. On the other hand, the amplitudes of the dominant frequencies for the sensor z_1 are amplified by both feedback and feedforward designs, leading to an increase of the H_2 norm for this transfer and thus an amplification upstream of the domain.

Indeed, reducing the amplitude of disturbances in one part of the frequency spectrum can lead to increasing it in the other part, which could predominate in other abscissas of the domain. Figure 16(c) shows the frequency spectrum of $S_{z_i w} = T^c_{z_i w}/T_{z_i w}$. For a sensor
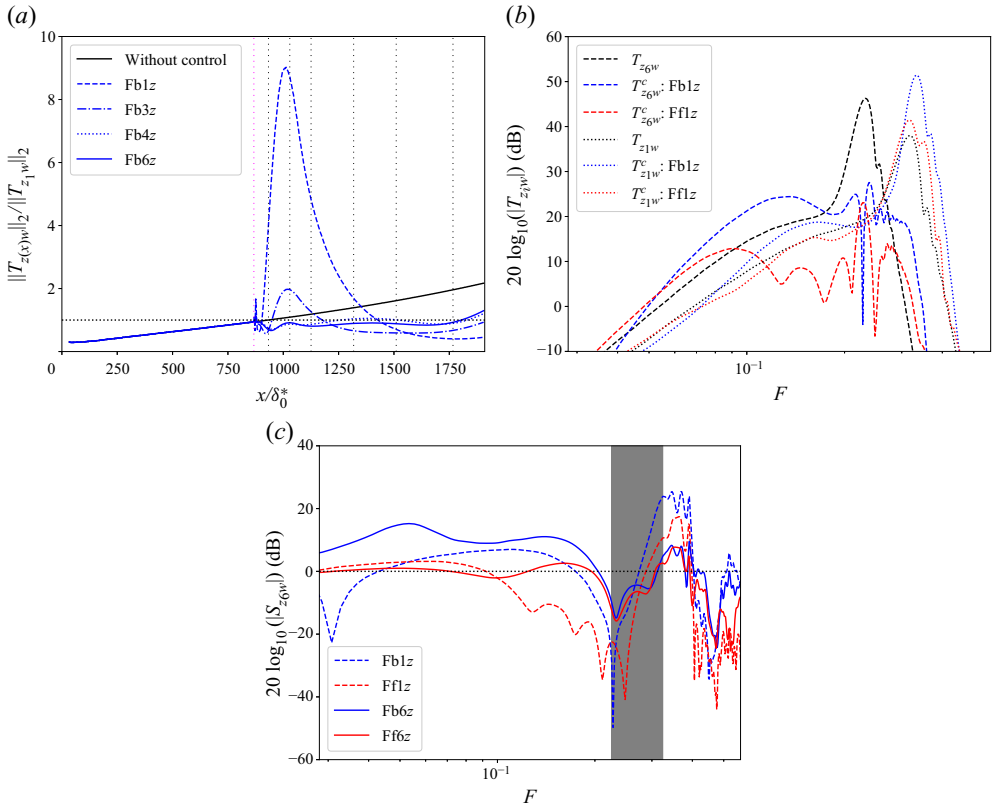
Figure 16. (*a*) Evolution of the local H_2 norm of the transfer $T_{z(x)w}$ from upstream noise w to wall-pressure fluctuation probes $z(x)$. The vertical magenta and black dotted lines represent, respectively, the position of the actuator (with the sensors y_{fb} and y_{ff} nearby) and the performance sensors z_i that can be used for synthesis. The values are normalized by $\|T_{z_1w}\|_2$. (*b*) Comparison of T_{z_6w} (solid lines) and T_{z_1w} (dashed lines) for the uncontrolled (black lines), Fb1z (blue lines) and Ff1z (red lines) cases. (*c*) Comparison of S_{z_6w} for different control cases. Disturbance rejection is improved (resp. degraded) below (resp. above) the dotted line. The grey shaded area represents the frequency range to be controlled from the actuator to the end of the domain.

z_i, disturbance rejection is achieved at frequencies where $|S_{z_iw}| < 1$. We can see from this figure that an effect similar to the waterbed effect (Skogestad & Postlethwaite 2005) appears: for the Fb1z and Ff1z cases, the significant disturbance rejection at frequencies around $F = 0.225$ is accompanied by an amplification for higher and lower frequencies. The frequency range to be controlled being around $F \in [0.225, 0.324]$ (see figure 5*b*), amplifying lower frequencies is not a problem in our case as these will be found further downstream of z_6 and therefore not taken into account in the computational domain. However, amplifying frequencies around $F = 0.324$ will directly impact performance on the sensor z_1, which is dominated by these frequencies. This translates into the need to use several sensors z_i in the synthesis to obtain a suitable frequency representation in different abscissas of the domain to avoid an unwanted waterbed effect. Both Fb6z and Ff6z cases have lower disturbance rejection at frequencies around $F = 0.225$, but the waterbed effect on high frequencies is mitigated compared to Fb1z and Ff1z cases (see figure 16*c*). By taking more and more performance sensors along the plate for the synthesis, we cover a wider spectrum of amplified frequencies. The larger the frequency range to be rejected, the more complicated it is to obtain very high attenuation on the spectrum. This is why the quantity $\max_{z_i \in z_{used}} \|T^c_{z_iw}\|_2$ increases with the number of performance sensors used in the

954 A20-36

synthesis (see table 2). Nevertheless, due to the better coverage of amplified frequencies by increasing the number of z_i used in the synthesis, a more uniform performance along the plate is obtained (see table 2 and figure 16a).

Taking three performance sensors (one near the actuator, one near the end of the domain, and another in between) and thus covering a wider frequency spectrum, the Fb3z case (dashed-dotted line in figure 16a) allows us to significantly reduce the local H_2 norm increase near the actuator compared to the Fb1z. However, immediately after the position of the sensor z_1 (first vertical black dotted line), yet taken into account in this synthesis, the local H_2 norm increases and a slight bump appears at $x \approx 1020\delta_0^*$. It is associated with strong non-modal effects in the vicinity of the actuator (see § 4.3). For frequencies around $F = 0.296$ – those dominant in the vicinity of the actuator – the modal behaviour is found only for $x \gtrsim 1136.4\delta_0^*$ (see figure 5d). Therefore, we need to discretize the area from the actuator to the end of the transient non-modal region with several performance sensors, as in the Fb4z and Fb6z cases. Because $\max_{x_1 < x < x_6} \| T_{z(x)w}^c \|_2$ is lower in the Fb6z case than in the Fb4z case due to a better coverage of the amplified frequency spectrum along the plate, six performance sensors are therefore used in the syntheses of § 6.

Appendix D. Control efficiency

We assess the control efficiency by looking at the coefficient:

$$
\Phi = \frac{\displaystyle\int_{\partial\Omega} \frac{1}{2}\langle e_{Chu} - e_{Chu}^c \rangle_t \, \bar{\boldsymbol{u}} \cdot \boldsymbol{n}\, \mathrm{d}s}{\displaystyle\int_{\Omega} \langle u(t)\, \boldsymbol{B}_u \cdot \boldsymbol{u}'^c \rangle_t \, \mathrm{d}\Omega}.
\tag{D1}
$$

As mean kinetic perturbation energy flux difference between the uncontrolled and controlled simulations is sometimes used in the incompressible case (Barbagallo *et al.* 2012), a mean Chu energy flux difference $\int_{\partial\Omega} \frac{1}{2}\langle e_{Chu} - e_{Chu}^c \rangle_t \, \bar{\boldsymbol{u}} \cdot \boldsymbol{n}\, \mathrm{d}s$ is chosen for our compressible boundary layer to compute the gain. The term $\int_{\Omega} \langle u(t)\, \boldsymbol{B}_u \cdot \boldsymbol{u}'^c \rangle_t \, \mathrm{d}\Omega$ represents the mean power spent by the user during the control effort (Barbagallo *et al.* 2012; Fabbiane, Bagheri & Henningson 2017). For Ω, the right boundary stops at x_6, while the left boundary is taken sufficiently upstream of the actuator position so that the uncontrolled and controlled flux at this boundary are identical. Moreover, the line integrals along the wall and the upstream boundary yield zero contributions, so the gain just represents the mean Chu energy flux difference at x_6. For the feedforward and feedback designs, $\Phi_{ff} = 555.5$ and $\Phi_{fb} = 109.1$, respectively. The feedforward design has a better energy efficiency than the feedback one, as one would expect because the feedforward controller reduces more the perturbation amplitude and has a lower control signal amplitude than the feedback one. Both configurations have a largely positive efficiency, which is due to the fact that the control takes advantage of the instability mechanism to cancel perturbations, leading to a low control effort (Barbagallo *et al.* 2012). This coefficient Φ based on mean Chu energy flux would be underestimated compared to realistic 3-D configurations where nonlinearities and transition start to occur at the end of Ω: delaying transition in Ω would lead to large gain, while keeping low control effort as the actuator would be placed in a weakly nonlinear area at its streamwise position to stay close to the linear on-design point. Nevertheless, the coefficient Φ may also be considered as overestimated because the forcing of the actuator would not necessarily be optimal in a realistic configuration (i.e. not centred around the generalized inflection point) and there
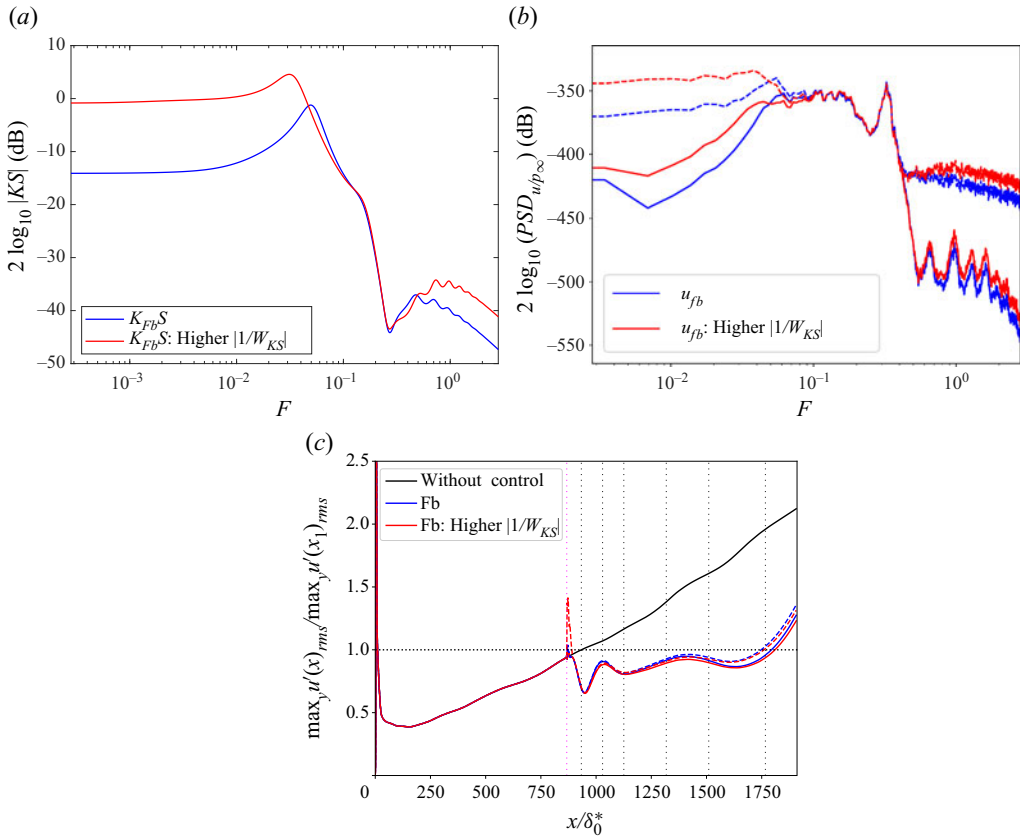
Figure 17. Comparison of (*a*) *KS*, (*b*) *PSD_u* and (*c*) max_y *u'_rms* for a feedback controller resulting from a synthesis with a higher $|1/W_{KS}|$ (red lines) than for the one used in § 6 (blue lines). Solid lines and dashed lines in (*b*) and (*c*) represent the cases with ideal and noisy estimation sensors, respectively. The caption for (*c*) is as for figure 8(*c*).

would be also electro-mechanical conversion losses. Indeed, the control cost between an ideal actuator (modelled by a volume forcing) and a realistic one (e.g. plasma actuator) may be very different (Fabbiane *et al.* 2017). Finally, in 3-D configurations where transition occurs, the gain would no longer be related to a mean Chu energy flux but would be computed in terms of saved drag (Stroh *et al.* 2015; Fabbiane *et al.* 2017), which makes the conclusions of a 2-D ideal numerical study difficult to exploit in terms of control efficiency.

Appendix E. Impact of W_{KS} on the performance with noisy estimation sensors

To illustrate the impact of the weighting function W_{KS} on the performance, the constraint minimization problem (5.3) is solved but with a higher $|1/W_{KS}|$ compared to the one use all along in § 6. The feedback controller resulting from this synthesis (red lines) is shown in figure 17(*a*) and is compared to the previous one used in § 6 (blue lines). The two controllers have globally the same behaviour in the bandwidth of the second Mack mode, but the new controller has higher gain in the low-frequency range. In the case where the estimation sensors are corrupted by the same amount of white Gaussian noise as in § 6.3 (50 % of the r.m.s. value without control of y_{fb}), it follows that the *u*-PSD for a corrupted

signal y becomes more important in low frequencies for the controller resulting from the synthesis with a higher $|1/W_{KS}|$ than for the previous controller (see figure 17*b*). For the noisy estimation sensor case, and contrary to the controller used all along in § 6, the new controller leads to a strong energy injection in the vicinity of the actuator (see the red dashed line in figure 17*c*). As these injected low frequencies are convectively stable, they attenuate very quickly, but the maximum along the wall-normal direction of u'_{rms} clearly exceeds the energy threshold before the last performance sensor z_i used in the synthesis, which could trigger the transition to turbulence in a 3-D configuration. It should be noted that in the case of ideal estimation sensors, the controller resulting from the synthesis with a higher $|1/W_{KS}|$ minimizes slightly more the velocity fluctuations compared to the previous feedback controller used in § 6 (see solid lines in figure 17*c*) because the constraint on W_{KS} is less important. There is therefore a trade-off between minimizing H_2 norms and desensitizing the controller in the low-frequency range during the synthesis.

REFERENCES

AMESTOY, P.R., DUFF, I.S., L'EXCELLENT, J.-Y. & KOSTER, J. 2001 *A fully asynchronous multifrontal solver using distributed dynamic scheduling*, vol. 23. SIAM.

APKARIAN, P., GAHINET, P. & BUHR, C. 2014 Multi-model, multi-objective tuning of fixed-structure controllers. In *2014 European Control Conference (ECC)*, pp. 856–861. IEEE.

APKARIAN, P. & NOLL, D. 2006 Nonsmooth H_∞ synthesis. *IEEE Trans. Autom. Control* **51**, 71–86.

APKARIAN, P., NOLL, D. & RONDEPIERRE, A. 2010 Mixed H_2/H_∞ control via nonsmooth optimization. In *Proceedings of the IEEE Conference on Decision and Control*, vol. 47, pp. 6460–6465. IEEE.

BAGHERI, S., BRANDT, L. & HENNINGSON, D.S. 2009 Input–output analysis, model reduction and control of the flat-plate boundary layer. *J. Fluid Mech.* **620**, 263–298.

BARBAGALLO, A., DERGHAM, G., SIPP, D., SCHMID, P.J. & ROBINET, J.-C. 2012 Closed-loop control of unsteadiness over a rounded backward-facing step. *J. Fluid Mech.* **703**, 326–362.

BARBAGALLO, A., SIPP, D. & SCHMID, P.J. 2009 Closed-loop control of an open cavity flow using reduced-order models. *J. Fluid Mech.* **641**, 1–50.

BELSON, B.A., SEMERARO, O., ROWLEY, C.W. & HENNINGSON, D.S. 2013 Feedback control of instabilities in the two-dimensional Blasius boundary layer: the role of sensors and actuators. *Phys. Fluids* **25**, 054106.

BENEDDINE, S. 2017 Characterization of unsteady flow behavior by linear stability analysis. PhD thesis, Université Paris-Saclay.

BENEDDINE, S., METTOT, C. & SIPP, D. 2015 Global stability analysis of underexpanded screeching jets. *Eur. J. Mech. (B/Fluids)* **49**, 392–399.

BUGEAT, B., CHASSAING, J.-C., ROBINET, J.-C. & SAGAUT, P. 2019 3D global optimal forcing and response of the supersonic boundary layer. *J. Comput. Phys.* **398**, 108888.

CAMBIER, L., HEIB, S. & PLOT, S. 2013 The Onera elsA CFD sofware: input from research and feedback from industry. *Mech. Ind.* **14**, 159–174.

CELEP, M., HADJADJ, A., SHADLOO, M.S., SHARMA, S., YILDIZ, M. & KLOKER, M.J. 2022 Effect of streak employing control of oblique-breakdown in a supersonic boundary layer with weak wall heating/cooling. *Phys. Rev. Fluids* **7**, 053904.

CHEN, J., ZHOU, K. & CHANG, B.-C. 1994 Closed-loop controller reduction by a structured truncation approach. In *Proceedings of 1994 33rd IEEE Conference on Decision and Control*, vol. 3, pp. 2726–2731. IEEE.

DADFAR, R., FABBIANE, N., BAGHERI, S. & HENNINGSON, D.S. 2014 Centralised versus decentralised active control of boundary layer instabilities. *Flow, Turbul. Combust.* **93**, 537–553.

DADFAR, R., SEMERARO, O., HANIFI, A. & HENNINGSON, D.S. 2013 Output feedback control of Blasius flow with leading edge using plasma actuator. *AIAA J.* **51**, 2192–2207.

DOYLE, J. 1978 Guaranteed margins for LQG regulators. *IEEE Trans. Autom. Control* **23**, 756–757.

DOYLE, J., GLOVER, K., KHARGONEKAR, P.P. & FRANCIS, B.A. 1989 State-space solutions to standard H_2 and H_∞ control problems. *IEEE Trans. Autom. Control* **34**, 831–847.

DOYLE, J. & STEIN, G. 1981 Multivariable feedback design: concepts for a classical/modern synthesis. *IEEE Trans. Autom. Control* **26**, 4–16.

DRMAC, Z., GUGERCIN, S. & BEATTIE, C. 2015 Quadrature-based vector fitting for discretized H_2 approximation. *SIAM J. Sci. Comput.* **2**, A625–A652.

ERDMANN, R., PÄTZOLD, A., ENGERT, M., PELTZER, I. & NITSCHE, W. 2011 On active control of laminar–turbulent transition on two-dimensional wings. *Phil. Trans. R. Soc.* A **369** (1940), 1382–1395.

FABBIANE, N., BAGHERI, S., & HENNINGSON, D.S. 2017 Energy efficiency and performance limitations of linear adaptive control for transition delay. *J. Fluid Mech.* **810**, 60–81.

FABBIANE, N., SEMERARO, O., BAGHERI, S. & HENNINGSON, D.S. 2014 Adaptive and model-based control theory applied to convectively unstable flows. *Appl. Mech. Rev.* **66**, 60801.

FABBIANE, N., SIMON, B., FISCHER, F., GRUNDMANN, S., BAGHERI, S. & HENNINGSON, D.S. 2015 On the role of adaptivity for robust laminar flow control. *J. Fluid Mech.* **767**.

FEDOROV, A. 2011 Transition and stability of high-speed boundary layers. *Annu. Rev. Fluid Mech.* **43**, 79–95.

FEDOROV, A. & TUMIN, A. 2022 The Mack's amplitude method revisited. *Theor. Comput. Fluid Dyn.* **36**, 9–24.

FLINOIS, T.L.B. & MORGANS, A.S. 2016 Feedback control of unstable flows: a direct modelling approach using the eigensystem realisation algorithm. *J. Fluid Mech.* **793**, 41–78.

FRANKLIN, G.F., POWELL, J.D. & WORKMAN, M.L. 1997 *Digital Control of Dynamic Systems – Third Edition*. Prentice Hall.

FREIRE, G.A., CAVALIERI, A.V.G., SILVESTRE, F.J., HANIFI, A. & HENNINGSON, D.S. 2020 Actuator and sensor placement for closed-loop control of convective instabilities. *Theor. Comput. Fluid Dyn.* **34**, 619–641.

GAD-EL HAK, M. 2000 *Flow Control: Passive, Active, and Reactive Flow Management*. Cambridge University Press.

GAPONOV, S.A. & SMORODSKY, B.V. 2016 Supersonic turbulent boundary layer drag control using spanwise wall oscillation. *Intl J. Theor. Appl. Mech.* **1**, 97–103.

GEAR, C.W. 1971 *Numerical Initial Value Problems in Ordinary Differential Equations*. Prentice-Hall.

GLAD, T. & LJUNG, L. 2000 *Control Theory*. Taylor & Francis.

GODDARD, P.J. & GLOVER, K. 1995 Performance-preserving controller approximation. PhD thesis, University of Cambridge.

HANIFI, A., SCHMID, P.J. & HENNINGSON, D.S. 1996 Transient growth in compressible boundary layer flow. *Phys. Fluids* **8**, 826.

HERVÉ, A., SIPP, D., SCHMID, P.J. & SAMUELIDES, M. 2012 A physics-based approach to flow control using system identification. *J. Fluid Mech.* **702**, 26–58.

HUERRE, P. & MONKEWITZ, P.A. 1990 Local and global instabilities in spatially developing flows. *Annu. Rev. Fluid Mech.* **22**, 473–537.

JAHANBAKHSHI, R. & ZAKI, T.A. 2021 Optimal heat flux for delaying transition to turbulence in a high-speed boundary layer. *J. Fluid Mech.* **916**, A46.

JUANG, J.-N. & PAPPA, R.S. 1985 An eigensystem realization algorithm for modal parameter identification and model reduction. *J. Guid. Control Dyn.* **8**, 620–627.

JUILLET, F., SCHMID, P.J. & HUERRE, P. 2013 Control of amplifier flows using subspace identification techniques. *J. Fluid Mech.* **725**, 522–565.

JULIANO, T.J., BORG, M.P. & SCHNEIDER, S.P. 2015 Quiet tunnel measurements of HIFiRE-5 boundary-layer transition. *AIAA J.* **53**, 1980–1993.

KALMAN, R. 1964 When is a linear control system optimal. *J. Basic Engng* **86**, 51–60.

KENDALL, J.M. 1975 Wind tunnel experiments relating to supersonic and hypersonic boundary-layer transition. *AIAA J.* **13**, 290.

KWAKERNAAK, H. 1969 Optimal low-sensitivity linear feedback systems. *Automatica* **5**, 279–285.

LECLERCQ, C., DEMOURANT, F., POUSSOT-VASSAL, C. & SIPP, D. 2019 Linear iterative method for closed-loop control of quasiperiodic flows. *J. Fluid Mech.* **868**, 22–65.

VAN LEER, B. 1979 Towards the ultimate conservative difference scheme. V. A second-order sequel to Godunov's method. *J. Comput. Phys.* **32**, 101–136.

LEHOUCQ, R., SORENSEN, D. & YANG, C. 1998 Arpack users' guide: solution of large scale eigenvalue problems with implicitly restarted Arnoldi methods. *SIAM* **6**.

LIOU, M.-S. 2006 A sequel to AUSM, Part II: Ausm$^+$-up for all speeds. *J. Comput. Phys.* **214**, 137–170.

LUGRIN, M., NICOLAS, F., SEVERAC, N., TOBELI, J.-P., BENEDDINE, S., GARNIER, E., ESQUIEU, S. & BUR, R. 2022 Transitional shockwave/boundary layer interaction experiments in the R2Ch blowdown wind tunnel. *Exp. Fluids* **63**, 46.

MA, Y. & ZHONG, X. 2003 Receptivity of a supersonic boundary layer over a flat plate. Part 1. Wave structures and interactions. *J. Fluid Mech.* **488**, 31–78.

MACK, L.M. 1977 Transition and laminar instability. *NASA Tech. Rep.* CP 153203.

MACK, L.M. 1984 Boundary-layer linear stability theory. AGARD Report No. 709.

MALIK, M.R. 1989 Prediction and control of transition in supersonic and hypersonic boundary layers. *AIAA J.* **27**, 1487–1493.

MCKELVEY, T. & HELMERSSON, A. 1996 State-space parametrizations of multivariable linear systems using tridiagonal matrix forms. In *Proceedings of 35th IEEE Conference on Decision and Control*, vol. 4, pp. 3654–3659. IEEE.

MORKOVIN, M.V. 1969 On the many faces of transition. In *Viscous Drag Reduction* (ed. C. Sinclair Wells). Springer US.

MORRA, P., SASAKI, K., HANIFI, A., CAVALIERI, A.V.G. & HENNINGSON, D.S. 2020 A realizable data-driven approach to delay bypass transition with control theory. *J. Fluid Mech.* **883**, A33.

OLAZABAL-LOUMÉ, M., DANVIN, F., MATHIAUD, J. & AUPOIX, B. 2017 Study on k–ω shear stress transport model corrections applied to rough wall turbulent hypersonic boundary layers. In *Seventh European Conference for Aeronautics and Space Sciences*. doi:10.13009/EUCASS2017-604.

ORR, W.F. 1907 The stability or instability of the steady motions of a perfect liquid and of a viscous liquid. Part II. A viscous liquid. *Proc. R. Irish Acad.* A **27**, 69–138.

RAMESH, A.V., UTKU, S. & GARBA, J.A. 1989 Computational complexities and storage requirements of some Riccati equation solvers. *J. Guid. Control Dyn.* **12**, 469–479.

SAINT-JAMES, J. 2020 Prévision de la transition laminaire–turbulent dans le code elsA. Extension de la méthode des paraboles aux parois chauffées. PhD thesis, Institut Supérieur de l'Aéronautique et de l'Espace (ISAE).

SASAKI, K., MORRA, P., CAVALIERI, A.V.G., HANIFI, A. & HENNINGSON, D.S. 2020 On the role of actuation for the control of streaky structures in boundary layers. *J. Fluid Mech.* **883**, A34.

SASAKI, K., MORRA, P., FABBIANE, N., CAVALIERI, A.V.G., HANIFI, A. & HENNINGSON, D.S. 2018*a* On the wave-cancelling nature of boundary layer flow control. *Theor. Comput. Fluid Dyn.* **32**, 593–616.

SASAKI, K., TISSOT, G., CAVALIERI, A.V.G., SILVESTRE, F.J., JORDAN, P. & BIAU, D. 2018*b* Closed-loop control of a free shear flow: a framework using the parabolized stability equations. *Theor. Comput. Fluid Dyn.* **32**, 765–788.

SCHMID, P.J. 2007 Nonmodal stability theory. *Annu. Rev. Fluid Mech.* **39**, 129–162.

SCHMID, P.J. & SIPP, D. 2016 Linear control of oscillator and amplifier flows. *Phys. Rev. Fluids* **1**, 040501.

SEMERARO, O., BAGHERI, S., BRANDT, L. & HENNINGSON, D.S. 2011 Feedback control of three-dimensional optimal disturbances using reduced-order models. *J. Fluid Mech.* **677**, 63–102.

SEMERARO, O., BAGHERI, S., BRANDT, L. & HENNINGSON, D.S. 2013*a* Transition delay in a boundary layer flow using active control. *J. Fluid Mech.* **731**, 288–311.

SEMERARO, O., PRALITS, J.O., ROWLEY, C.W. & HENNINGSON, D.S. 2013*b* Riccati-less approach for optimal control and estimation: an application to two-dimensional boundary layers. *J. Fluid Mech.* **731**, 394–417.

SHAQARIN, T., OSWALD, P., NOACK, B.R. & SEMAAN, R. 2021 Drag reduction of a D-shaped bluff-body using linear parameter varying control. *Phys. Fluids* **33**, 077108.

SHARMA, S., SHADLOO, M.S., HADJADJ, A. & KLOKER, M.J. 2019 Control of oblique-type breakdown in a supersonic boundary layer employing streaks. *J. Fluid Mech.* **873**, 1072–1089.

SIPP, D., MARQUET, O., MELIGA, P. & BARBAGALLO, A. 2010 Dynamics and control of global instabilities in open-flows: a linearized approach. *Appl. Mech. Rev.* **63**, 030801.

SIPP, D. & SCHMID, P.J. 2016 Linear closed-loop control of fluid instabilities and noise-induced perturbations: a review of approaches and tools. *Appl. Mech. Rev.* **68**, 020801.

SKOGESTAD, S. & POSTLETHWAITE, I. 2005 *Multivariable Feedback Control: Analysis and Design*. Wiley & Son.

SMITH, A.M.O. & GAMBERONI, N. 1956 *Transition, Pressure Gradient and Stability Theory*. Douglas Aircraft Company.

STROH, A., FROHNAPFEL, B., SCHLATTER, P. & HASEGAWA, Y. 2015 A comparison of opposition control in turbulent boundary layer and turbulent channel flow. *Phys. Fluids* **27** (7), 075101.

TOL, H.J., KOTSONIS, M. & DE VISSER, C.C. 2019 Pressure output feedback control of Tollmien–Schlichting waves in Falkner–Skan boundary layers. *AIAA J.* **57**, 1–14.

TOL, H.J., KOTSONIS, M., DE VISSER, C.C. & BAMIEH, B. 2017 Localised estimation and control of linear instabilities in two-dimensional wall-bounded shear flows. *J. Fluid Mech.* **824**, 818–865.

VEMURI, S.H.S., BOSWORTH, R., MORRISON, J.F. & KERRIGAN, E.C. 2018 Real-time feedback control of three-dimensional Tollmien–Schlichting waves using a dual-slot actuator geometry. *Phys. Rev. Fluids* **3**, 053903.

YAO, J. & HUSSAIN, F. 2019 Supersonic turbulent boundary layer drag control using spanwise wall oscillation. *J. Fluid Mech.* **880**, 388–429.

ZHANG, Z. & FREUDENBERG, J.S. 1987 Loop transfer recovery with non-minimum phase zeros. In *26th IEEE Conference on Decision and Control*, vol. 26, pp. 956–957. IEEE.